The Role of Coupled Sea Surface Temperatures in the Simulation of the Tropical Intraseasonal Oscillation

Y. ZHENG AND D. E. WALISER

Marine Sciences Research Center, State University of New York at Stony Brook, Stony Brook, New York

W. F. STERN

Geophysical Fluid Dynamics Laboratory, Princeton University, Princeton, New Jersey

C. JONES

Institute for Computational Earth System Science, University of California, Santa Barbara, Santa Barbara, California

(Manuscript received 1 August 2003, in final form 24 May 2004)

ABSTRACT

This study compares the tropical intraseasonal oscillation (TISO) variability in the Geophysical Fluid Dynamics Laboratory (GFDL) coupled general circulation model (CGCM) and the stand-alone atmospheric general circulation model (AGCM). For the AGCM simulation, the sea surface temperatures (SSTs) were specified using those from the CGCM simulation. This was done so that any differences in the TISO that emerged from the two simulations could be attributed to the coupling process and not to a difference in the mean background state. The comparison focused on analysis of the rainfall, 200-mb velocity potential, and 850-mb zonal wind data from the two simulations, for both summer and winter periods, and included comparisons to analogous diagnostics using NCEP–NCAR reanalysis and Climate Prediction Center (CPC) Merged Analysis of Precipitation (CMAP) rainfall data.

The results of the analysis showed three principal differences in the TISO variability between the coupled and uncoupled simulations. The first was that the CGCM showed an improvement in the spatial variability associated with the TISO mode, particularly for boreal summer. Specifically, the AGCM exhibited almost no TISO variability in the Indian Ocean during boreal summer—a common shortcoming among AGCMs. The CGCM, on the other hand, did show a considerable enhancement in TISO variability in this region for this season. The second was that the wavenumber–frequency spectra of the AGCM exhibited an unrealistic peak in variability at low wavenumbers (1–3, depending on the variable) and about 3 cycles yr^{-1} (cpy). This unrealistic peak of variability was absent in the CGCM, which otherwise tended to show good agreement with the observations. The third difference was that the AGCM showed a less realistic phase lag between the TISO-related convection and SST anomalies. In particular, the CGCM exhibited a near-quadrature relation between precipitation and SST anomalies, which is consistent with observations, while the phase lag was reduced in the AGCM by about 1.5 pentads (~1 week). The implications of the above results, including those for the notions of ''perfect SST'' and ''two tier'' experiments, are discussed, as are the caveats associated with the study's modeling framework and analysis.

1. Introduction

The dominant form of intraseasonal variability occurring in the tropical atmosphere is associated with what is often referred to as the intraseasonal oscillation (ISO) or Madden–Julian oscillation (MJO; e.g., Madden and Julian 1971, 1994). In recent years, the interaction of the MJO/ISO and the near-surface ocean has become an increasingly important consideration with regard to our understanding of both weather and climate and our ability to simulate them. This is due to the MJO/ISO's extensive interactions with other components of our weather/climate system, in conjunction with evidence that air–sea coupling may play an important role in defining the characteristics of the MJO/ISO. In terms of the former, the onset and break activity of the Asian–Australian monsoon system is strongly influenced by the propagation and evolution of MJO/ISO events (e.g., Hendon and Liebmann 1990a,b; Lau and Chan 1986b; Yasunari 1980). The development of persistent North Pacific circulation anomalies during boreal winter, and their influence on extreme precipitation events along the western United States, has been linked to the evolution

Corresponding author address: Dr. Duane E. Waliser, Jet Propulsion Laboratory, MS 183-505, California Institute of Technology, 4800 Oak Grove Drive, Pasadena, CA 91109.
E-mail: duane.waliser@jpl.nasa.gov

and eastward progression of convective anomalies associated with the MJO/ISO (e.g., Higgins and Mo 1997; Higgins et al. 2000; Higgins and Schubert 1996; Jones 2000; Lau and Phillips 1986; Liebmann and Hartmann 1984; Mo and Higgins 1998b,c; Weickmann 1983; Weickmann et al. 1985). Similarly, MJO/ISO convective activity has been linked to Northern Hemisphere (NH) summertime precipitation variability over Mexico and South America as well as to austral wintertime circulation anomalies over the Pacific–South American sector (e.g., Jones and Schemm 2000; Mo 2000; Mo and Higgins 1998a; Nogues-Paegle and Mo 1997; Paegle et al. 2000). Studies have also shown that particular phases of the MJO are more favorable to the development of tropical storms/hurricanes in both the Atlantic and Pacific sectors (Higgins and Shi 2001; Maloney and Hartmann 2000a,b). Finally, the passage of MJO events over the western Pacific Ocean has been found to significantly modify the thermocline structure in the equatorial eastern Pacific Ocean via its connection to westerly wind bursts (e.g., Hendon et al. 1998; Kessler et al. 1995; McPhaden et al. 1988; McPhaden and Taft 1988). This latter interaction has even been suggested to play an important role in triggering variations in El Niño–Southern Oscillation (ENSO; e.g., Kessler and Kleeman 2000; Kessler et al. 1995; Lau and Chan 1986a; McPhaden 1999; Weickmann 1991).

It is important to point out at this stage that in regard to most of the processes and interactions highlighted above, the character of atmospheric intraseasonal variability is strongly dependent on season (Wang and Rui 1990; Jones et al. 2004). In the Northern Hemisphere winter, the dominant form of intraseasonal variability is most often referred to as the MJO (e.g., Hendon and Salby 1994). The canonical feature of the MJO involves large-scale convective anomalies that propagate eastward from the Indian Ocean, across the Maritime Continent and western Pacific, and into the South Pacific convergence zone (SPCZ). In contrast, the NH summertime intraseasonal variability, which has recently been most often referred to as the ISO to distinguish it from the MJO, involves large-scale convective events that appear to propagate northeastward from the Indian Ocean across Southeast Asia, into the northwestern tropical Pacific Ocean (Krishnamurti and Ardunay 1980; Sikka and Gadgil 1980), although the details of this propagation are more complex than suggested here (Kemball-Cook and Wang 2001; Annamalai and Slingo 2001). To help avoid confusion in regard to the above naming conventions and their implications for seasonality, we will, henceforth, refer to the combined form of intraseasonal variability that these two modes (e.g., MJO and ISO) represent as the tropical intraseasonal oscillation (TISO). Moreover, when referring to tropical intraseasonal variability that occurs during NH winter, we will either refer to this as the wintertime TISO or the MJO. Likewise, when referring to tropical intraseasonal variability that occurs during summer, we will either refer to this as summertime TISO or the ISO.

There is a growing interest in the role that sea surface temperatures (SSTs) may play in the simulation, maintenance, and propagation of the TISO. Most theoretical studies of the TISO have typically addressed the winter mode (i.e., MJO) and have assumed a background state in which SSTs remain fixed (Emanuel 1987; Neelin et al. 1987; Lau and Peng 1987; Chang and Lim 1988; Hendon 1988). Hence, coupled processes between TISO-modulated surface heat fluxes and the SSTs have not been accounted for. These theoretical studies have often had difficulties representing some of the salient features of the MJO (e.g., proper phase speed). In addition, general circulation model (GCM) studies of the MJO, which have most often been undertaken under conditions of specified SSTs, have indicated that obtaining realistic simulations of the TISO can be especially challenging at best and yet unattainable at worst (e.g., Slingo et al. 1996; Waliser et al. 2003a). Common shortcomings in terms of the TISO in AGCMs include weak intraseasonal variability, unrealistic phase speeds, poor seasonality, etc. Given the significant variability in surface heat fluxes and SSTs on intraseasonal time scales (e.g., Krishnamurti et al. 1988; Zhang 1996; Lau and Sui 1997; Jones et al. 1998; Hendon and Glick 1997), which appear to be TISO driven, this has led to the speculation that interactive SSTs may play an important role in the observed TISO and may in part be responsible for the poor simulation of TISO by AGCMs with fixed SSTs (e.g., Kawamura 1988; Jones and Weare 1996; Waliser 1996; Sperber et al. 1997).

Results from the Tropical Ocean Global Atmosphere Coupled Ocean–Atmosphere Response Experiment (TOGA COARE) (Webster and Lukas 1992) indicate that the variability in precipitation and cloud, to some degree, is strongly controlled by the MJO (Johnson 1995). Therefore, the MJO can regulate shortwave radiative heating in the ocean mixed layer via changing cloudiness. Strong turbulent mixing and entrainment as well as latent heat loss associated with westerly wind bursts during the wet phase of winter TISO may also result in considerable cooling of the mixed layer. From TOGA and other studies, it is now well established that on intraseasonal time scales, positive SST anomalies lead convective anomalies by about one-quarter of a period (e.g., Kawamura 1988; Nakazawa 1995; Zhang 1996; Jones et al. 1998; Shinoda and Hendon 1998; Shinoda et al. 1998; Woolnough et al. 2000). Meanwhile, precipitable water vapor and convective available potential energy tend to follow SST variation and lead convection anomalies (Chou et al. 1995; Fasullo and Webster 1995). Taken together, the results of these studies suggest that variation of SSTs on intraseasonal time scales have the potential to significantly impact the MJO and possibly provide a positive feedback (Lau et al. 1997; Jones et al. 1998) in which SST variations may strengthen the power of the oscillation and influence its

eastward propagation (e.g., Kawamura 1991; Li and Wang 1994; Waliser 1996; Jones and Weare 1996; Flatau et al. 1997; Lau and Sui 1997; Sperber et al. 1997). Similar analyses and arguments have been put forth regarding the summertime ISO (e.g., Vecchi and Harrison 2000; Kemball-Cook and Wang 2001; Sengupta and Ravichandran 2001; Sengupta et al. 2001).

At present, there are a number of modeling studies that explore the relationship between SST coupling and the TISO. Below, we highlight a few of the studies that are most obviously relevant to the work described here (see also Watterson 2002; Sobel and Gildor 2003; Maloney and Kiehl 2002). By using a five-layer, idealized, R15 atmospheric model over an ''aquaplanet'' with a simplified surface energy budget and ocean mixed layer feedback, Flatau et al. (1997) discussed the feedback between SST changes produced by equatorial convection and the dynamics of the intraseasonal oscillation. They found that, while the uncoupled model produced relatively fast, incoherent MJO-like variability, the inclusion of interactive SSTs produced a more organized, stronger, and slower MJO. They suggest that this occurred as a result of positive SST anomalies to the east of the convective anomalies that served to destabilize the atmosphere by increasing the moist static energy.

Wang and Xie (1998) investigated the roles of the air–sea interaction in the warm pool in maintaining the MJO by emphasizing ocean mixed layer physics and thermodynamic coupling in a theoretical modeling study. As a result of coupling, the modeled MJO had a more realistic eastward propagation speed. This occurred due to a phase relationship between SST anomalies and MJO-induced convective anomalies, in that the former leads the latter by about a quarter cycle. Meanwhile, the positive SST anomalies were in phase with surface low pressure, which decreased the surface pressure and hence increased zonal wind convergence into the convective anomalies. Contrary to Flatau et al. (1997), without coupling to the ocean mixed layer, there were no unstable modes found in the modeled atmosphere.

Waliser et al. (1999b) found that when their AGCM was coupled to a slab of ocean mixed layer, the interactive SSTs had modest but important impacts in the simulation of the MJO, with the characteristics of the coupled model's MJO being closer to those observed. These impacts included 1) the increased variability associated with the MJO, 2) the tendency for the time scales of modeled intraseasonal variability to be around those found in the observations, 3) a reduced eastward phase speed in the Eastern Hemisphere, and 4) an increased seasonal signature in the MJO with relatively more events occurring in the December–May period. They attributed the better simulation to the feedback with the SSTs. They suggested that the enhanced SSTs, forced by decreased latent heating and increased short wave flux to the east of the positive convective anomalies, tended to reinforce the meridional convergence associated with the frictional wave-CISK mechanism working within the AGCM. This meridional convergence increased the moist static energy that acts to destabilize the model's MJO.

Hendon (2000) explored the impact of air–sea coupling on the dynamics of the MJO in a GCM with coupling to a one-dimensional ocean mixed layer model. In that study, Hendon found that coupling had no significant influence on the simulation of the MJO. However, analysis of the model results showed that the simulated MJO-induced latent heat flux anomalies were relatively incoherent and did not exhibit the proper (i.e., observed) phase relationship relative to the convection, in part due to the model's basic state. Thus, the latent heat flux anomalies did not constructively interact with the MJO-induced shortwave anomalies to produce the needed/observed systematic changes in the anomalous SST that in turn could influence the MJO. Thus, to some degree, this study's findings highlight the necessity for a proper representation of the basic state when simulating the MJO rather than having implications on the SST–MJO coupling question directly. Additional important work in this area includes the studies by Inness and Slingo (2003) and Inness et al. (2003) that emphasize the basic state in terms of having westerly low-level zonal winds present in regions where eastward propagation is observed/expected (e.g., Indian and western Pacific Oceans).

In a recent study focusing on summertime TISO variability, Kemball-Cook et al. (2002) examined the simulation of the intraseasonal oscillation in the ECHAM-4 model and found a pronounced northward propagation of convection and circulation anomalies over the Indian Ocean in the May–June Asian monsoon season when the AGCM was coupled to the 2.5-layer ocean model, which is consistent with the observations. In concert with most of the studies above, this improvement was primarily due to air–sea interaction that acts to increase low-level convergence into the warmer SST anomalies ahead of the convective anomalies. However, the coupled model failed to produce the August–October observed northwestward propagation of convection anomalies due to the absence of easterly vertical shear (due to shortcomings in the basic state) that is crucial for the emission of Rossby waves, while the uncoupled run did produce this northwestward propagation of convection anomalies since the SSTs were specified from the observations and therefore generated a realistic easterly vertical shear.

Wu et al. (2002) employed 10-member ensemble simulations with 10 different AGCMs forced with the same observed weekly SSTs but with different initial atmospheric conditions to explore the intraseasonal variability in the South Asian monsoon region during 1996–98. Apart from finding considerable differences in the ability of the models to capture the observed features of the TISO, they performed a case study of a particularly strong MJO event in the model and observed

records. One of the main findings in that analysis relevant to the present study is that while the observed convection anomalies were in quadrature with, and lagging, the associated intraseasonal anomaly in SST, the simulated MJO convection events were nearly in phase with the SST anomaly. Based on the results of the studies mentioned above, the observed relationship is understood to come about—to first order—via TISO-driven heat flux variations imparting an intraseasonal signal on SST. However, given the specified SST framework of the observations, the modeled relationship is more accurately depicted as a ''forced'' signal whereby the TISO event is responding to the SST variations in the boundary conditions. These results help to emphasize the coupled nature of the TISO and the importance of treating it as a coupled phenomenon in the context of numerical simulations.

In an extension of the Kemball-Cook et al. study, Fu et al. (2003) used an improved version of the ECHAM-4 coupled model and a model framework analogous to that used here. This latter aspect greatly improved the robustness of the earlier study because comparisons of the coupled and uncoupled models could be made with the same basic state in order to isolate the impact from just the coupling (e.g., Waliser et al. 1999b). The results of their study provided further evidence that SST coupling was a necessary component in order to produce realistic northward-propagating TISO phenomena during boreal summer, including proper phasing relative between the convection and SST anomalies. In addition, they showed that the preference for northward propagation during boreal summer was tied to the nature of the boreal summer basic state in conjunction with coupled processes.

The goal of the present study is to continue to explore the role that the SST coupling plays in the simulations of the TISO. Due to our use of a fully coupled ocean GCM and the use of a model that has yet to be explored in regards to this phenomenon, our study extends those models highlighted above. In particular, our objective is to investigate the sensitivity of the TISO to the coupled versus uncoupled SST condition. This includes an assessment of both NH summer and winter conditions (i.e., both the wintertime MJO and summertime ISO). To this end, we utilize the Geophysical Fluid Dynamics Laboratory (GFDL) GCM that has been shown to exhibit relatively robust intraseasonal variability (e.g., Waliser et al. 2003a). From the resulting simulations, we examine the TISO variability in terms of strength, wavenumber–frequency spectrum, spatial and temporal evolution, phase relation to SST, etc. From this analysis, we determine whether the influences from the coupled SST on the TISO fall within any of the categories of results from the previous studies described above. In addition, we compare the modeled results with observations to assess the realism of the model simulations. In the next section, a detailed description of the model will be presented. In section 3, the model results are to be presented. We summarize our study in section 4.

2. Model and experiments

Experiments used in our study include both the GFDL coupled GCM (CGCM) and AGCM. The atmospheric model, described in detail by Stern and Miyakoda (1995), is a global spectral GCM with T42 truncation and 18 sigma levels. Physical parameterizations in the atmospheric model include a bucket hydrology; orographic gravity wave drag; large-scale condensation; relaxed Arakawa–Schubert (RAS) convection; shallow convection; cloud prediction; radiative transfer (2-h averaged); stability dependent vertical eddy fluxes of heat, momentum, and moisture throughout the surface layer; planetary boundary layer; and free atmosphere and horizontal diffusion. The orography has been treated by a Gibbs oscillation reduction method.

The ocean model used is GFDL's modular ocean model, version 1, MOM2, configured with a nearly global grid with realistic bottom topography and horizontal resolution of 1° latitude $\times$ 1° longitude except within the equatorial band of 10°N–10°S, where the meridional resolution is 1/3°. The vertical resolution is 15 unequally spaced levels, with most of the levels in the upper ocean above 500 m. Some of the key features of the physics include penetration of solar insolation to the ocean subsurface, Pacanowski–Philander vertical mixing, and constant horizontal mixing (Pacanowski 1995).

There are two types of simulations examined in the present study. The first simulation, the CGCM, is based on the GFDL atmosphere–ocean coupled GCM. These coupled sets of experiments were derived from six-member ensembles of the coupled ocean–atmosphere GCM predictions that were generated starting from 1 January (1 July) of each year from 1980 (1979) through 1997. Initial conditions for the ocean were produced by the GFDL ocean data assimilation system that uses the MOM2 ocean model, forced by observed wind stresses, and assimilated observed SSTs and subsurface thermal data. Atmospheric initial conditions were taken from six long-term integrations of the AGCM forced by the SSTs from the ocean data assimilation. Ensembles of six 1-yr CGCM predictions were initiated at each 1 January (1 July) by using each of the six AGCM solutions, to define the state of the atmosphere and land surface from 1980 (1979) through 1997. In this study, we use a single, arbitrarily chosen member from the six-member ensembles. The cases starting on 1 January (1 July) will be used for the boreal summer (winter) TISO analysis.

In the coupled simulation, the atmosphere is integrated for 2 h (with an 80-s time step), and then averages of these 2-h segments of wind stress, heat flux, and precipitation minus evaporation are used to force the ocean model. Then the ocean model is run for 2 h (with a 1-h time step) with averages of these 2-h segments of SST used in the subsequent integration of the atmo-

spheric model. The second simulation, the AGCM, is based on the GFDL's AGCM forced by the fixed daily SSTs obtained from the coupled model simulation discussed above.

From each set of simulations described above, we analyze daily mean values of velocity potential (VP) at 200 mb (VP200), zonal winds at 850 mb (U850), surface temperature, and precipitation. Note that the daily mean precipitation data are actually 18-h (0600–0000) means not 24-h means. The observational datasets used in this study include the global pentad Climate Prediction Center (CPC) Merged Analysis Precipitation (CMAP) constructed by Xie and Arkin on a 2.5° latitude $\times$ 2.5° longitude grid from 1979 to 2001 (e.g., Xie and Arkin 1997). We also employ 200-mb velocity potential, and 850-mb zonal winds from the National Centers for Environmental Prediction–National Center for Atmospheric Research (NCEP–NCAR) reanalysis (Kalnay et al. 1996). For each of the observed datasets, only the period from 1979 to 1997 is used for comparison to the model simulations. For the purpose of evaluating the TISO, the analysis is restricted to 30°N–30°S and in some cases includes 30–90-day filtering (hereafter referred to as filtered data) using a 101-point 30–90-day Lanczos filterer (e.g., Duchon 1979). In order to distinguish and assess boreal summer and boreal winter TISO variability, summer (winter) in this study is defined to be May through October (November through April).

The purpose of our experiment design is to keep the daily SSTs the same between CGCM and AGCM. Thus, we rule out the influences from different background climate states in comparing the TISO to the coupled and uncoupled models (Waliser et al. 1999b). By comparing the CGCM with the AGCM, we can assess the importance of only the SST coupling in the simulation of the modeled TISO. However, it should be noted that while the daily SST values are the same, given the simulation framework described above, there is diurnal variability allowed over the ocean in the CGCM that is not included in the AGCM because of the use of specified daily SSTs. The shortcomings and caveats associated with this will be discussed in the summary. It should be noted that while the initial conditions for the corresponding AGCM and CGCM simulations are the same, it is this quantitative difference in the diurnal SST variability between the two simulations that allows them to evolve on different trajectories. Keep in mind that the analysis for a given simulation event is well removed from the initial start time of the integrations; for example, summer events are analyzed from simulations that started in January. Thus, any similarities in terms of the timing or nature of events from the two simulations derive from the boundary forcing and not the initial conditions.

3. Results

a. Mean climate

Figure 1 shows the 19-yr mean winter SST, rainfall, 200-mb VP, and 850-mb zonal wind from the CGCM simulation and observations. This figure indicates that the CGCM captures a number of global-scale features of the observed winter mean climate. For example, the distribution of the winter mean of precipitation for CGCM, as a whole, exhibits an extended west–east band south of the equator along with a generally correct wavenumber-1 pattern in the 200-mb VP. However, apart from these global-scale features, the model does exhibit considerable systematic biases relative to the observations on basinwide and regional scales. The main difference is in the detailed structure of the rainfall band(s) in the tropical Pacific and the influence this has on the circulation in these regions. For example, the model displays no component of the ITCZ north of the equator in the Pacific Ocean, and the SPCZ extension is too long and runs too parallel to the equator. The second largest difference is probably the considerably stronger precipitation around the Maritime Continent and Andes in the model as compared to the observations. Finally, while the low-level wind pattern in the Eastern Hemisphere exhibits fairly good agreement with the observations, the pattern over the central and eastern Pacific is quite poor in relation to the observations. The above differences can be mostly attributed to the considerable biases in the CGCM SSTs, which include a more meridionally confined warm pool in the Indian Ocean and western Pacific sector, with the regions north of the equator being too cold by up to about 2°C. On the other hand, the CGCM SSTs in the central and eastern Pacific exhibit a considerable warm bias, with values ranging from about 2°C north of the equator to as high as 4°C on and to the south of the equator.

Figure 2 is the same as Fig. 1 except for the summer. In this case, the overall global-scale pattern of precipitation from the CGCM is similar to the observation, probably more so than for the winter case, although the modeled precipitation rate is considerably weaker (~30% or more) than the observed over much of the Tropics, particularly in the Indian Ocean (~50% or more; e.g., Kang et al. 2002; Waliser et al. 2003a). One notable discrepancy with observations is the tendency for the CGCM to precipitate heavily over land areas of the summer monsoons (e.g., Southeast Asia, Central America) and to precipitate too lightly over the nearby ocean regions. When considered together, the above regional discrepancies make for somewhat poor agreement in the Asian/Indian sector. Corresponding to the relatively weaker rainfall, particularly in the Eastern Hemisphere, the circulation as illustrated by the 200-mb VP and 850-mb zonal wind is weaker than the observed, but otherwise they exhibit somewhat realistic mean patterns. The slightly better model–data agreement for the atmospheric fields for the summer versus winter cases reflects the fact that the bias in the CGCM SSTs over the Tropics as a whole is considerably and uniformly smaller than for the winter case. The main discrepancy in SST is a warm (cold) bias of about 2°C in the eastern Pacific (southern Indian) Ocean.

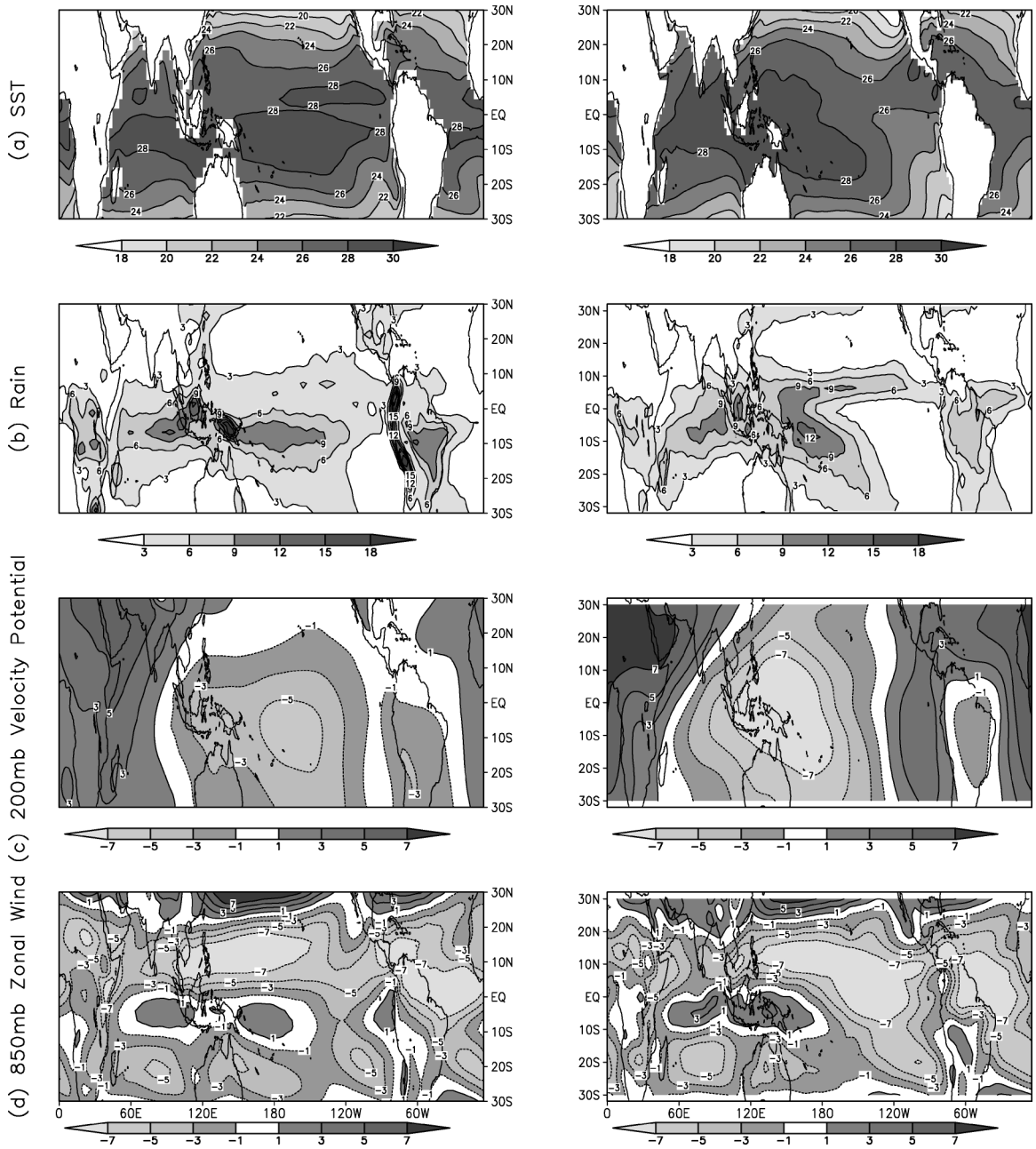

FIG. 1. Long-term winter (Nov–Apr) means of (a) SST, (b) rain rate, (c) VP200, and (d) U850 from the (left) CGCM simulation and from (right) observations. The model fields are winter means for the years 1979 through 1997 using the simulations starting in Jul (see section 2). The observed precipitation is from the global pentad CMAP from the period Jan 1979 to Dec 1997. The VP200 and U850 fields are from the NCEP–NCAR reanalysis (Kalnay et al. 1996) from the period 1979 to 1997. Units are °C for the temperature, mm day^{-1} for rain rate, 1×10^6 m^2 s^{-1} for VP, and m s^{-1} for zonal wind.

Figure 3 shows the differences in the mean rainfall, 200-mb VP, and 850-mb zonal winds between the CGCM and AGCM for both winter and summer. Highlighted are the areas that are 95% statistically significant using a Student's *t* test. Note also that the contour intervals in Fig. 3 are half the values used in Figs. 1 and 2. The maps illustrate that the AGCM and CGCM seasonal means are virtually the same, and that the differences that do show up are quite small, limited in spatial extent, and/or in many cases remote from the principal region of interest. This result should not come as too much of a surprise given that both the coupled and uncoupled atmosphere were forced by the same SST. However, it is worth emphasizing that it also indicates that the coupling process itself did not influence the means nor were there any significant low-frequency rec-

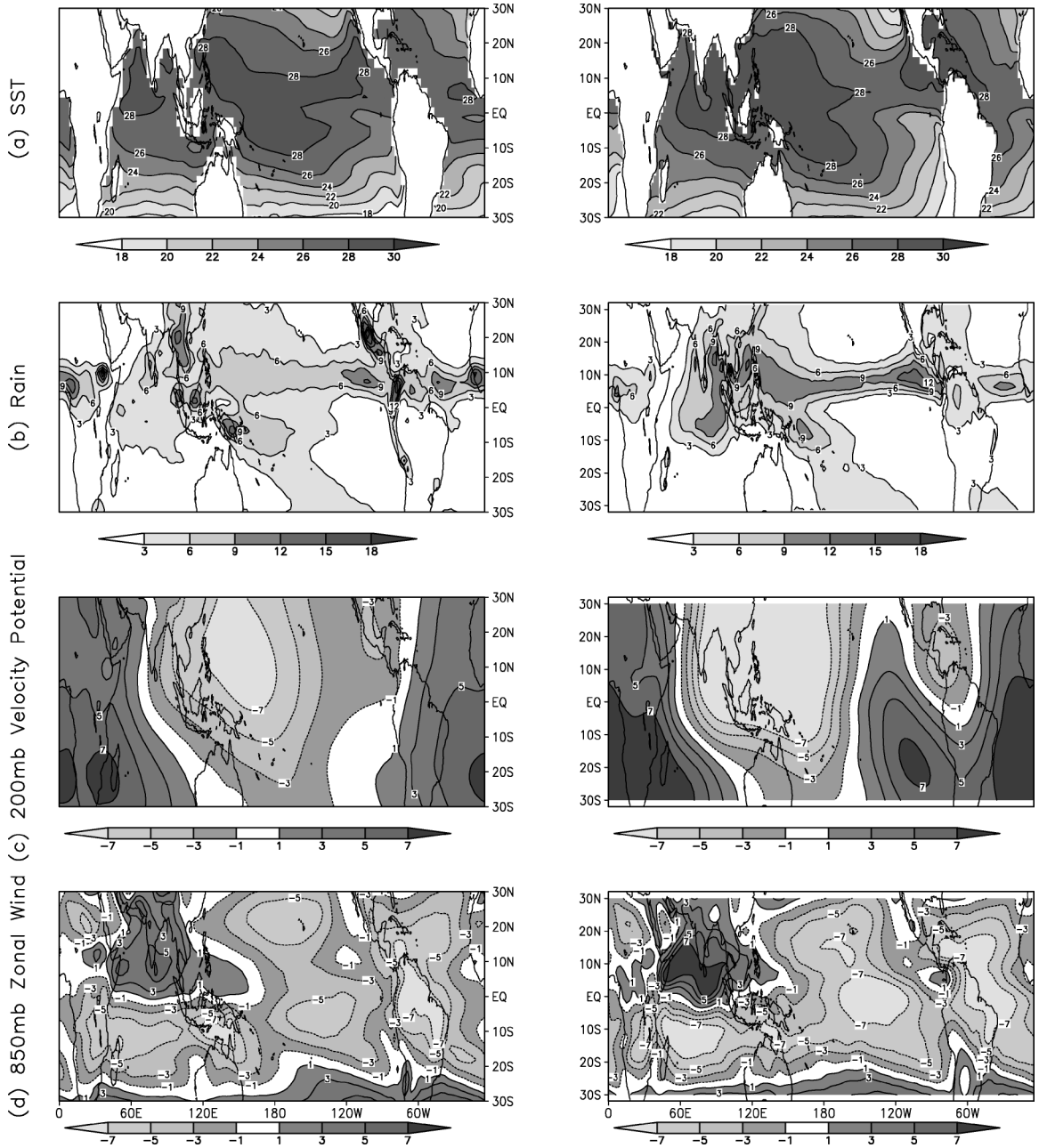

FIG. 2. Same as in Fig. 1, except for summer (May–Oct) means, for the period 1980 to 1997, and for simulations starting in Jan (see section 2).

tification effects onto the mean from time scales that did show sensitive to the coupling (i.e., TISO, see results below). Thus, based on Fig. 3, it can be concluded that the inclusion of interactive SSTs had little impact on the mean model climate, and therefore changes in TISO variability between the AGCM and CGCM can be attributed to the coupling itself rather than a change in the background state. Finally, in regards to the above model–data comparisons, and in particular their disagreement, it should be stressed that most of the variability associated with TISO occurs/originates in the Eastern Hemisphere, where there is relatively better model–data agreement. Moreover, the focus of this study is on the transient variability and not the mean, albeit they are related.

b. Intraseasonal variability

Figure 4 displays the spatial structure of the standard deviation of the filtered winter rainfall rate, 200-mb VP,

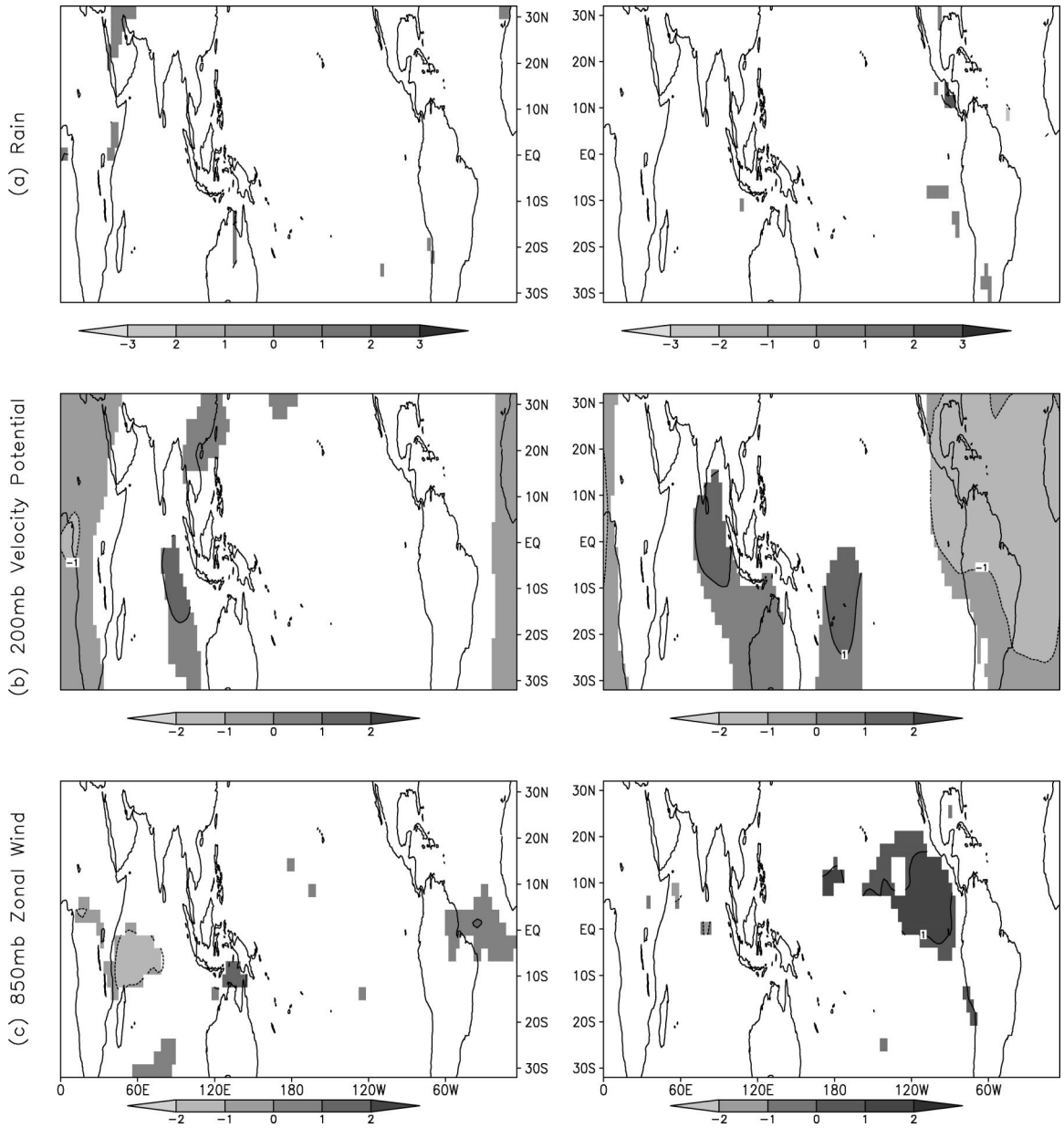

FIG. 3. The CGCM minus AGCM differences of long-term (left) winter and (right) summer means of (a) rain rate, (b) VP200, and (c) U850. Only the significant differences at the 95% confidence level, based on a Student's *t* test, are shown. Units are mm day^{-1} for rain rate, 1×10^6 m^2 s^{-1} for VP, and m s^{-1} for zonal wind.

and 850-mb zonal winds derived from the CGCM experiments and the observations. The modeled 30–90-day rainfall variability in winter is mostly located just south of the equator over the tropical Indian Ocean, Maritime Continent, western and central Pacific, and South America. The magnitude of the variability is stronger than the observations, especially over the Maritime Continent and Indian Ocean. Not surprisingly, the standard deviation of modeled filtered 200-mb VP in winter is considerably stronger than the observed 200-mb VP; over the Indian Ocean and Maritime Continent, there is about a 20% increase. Similarly, the standard deviation of filtered 850-mb zonal winds for the model is about 50% stronger than the observations, especially over the subtropical southern Indian Ocean, Maritime Continent, and regions to the east of date line. As the patterns of variability at this time scale roughly mimic the seasonal mean patterns (i.e., Fig. 1), the errors in the spatial distribution largely result from the nontrivial errors in the basic state of the SST that were discussed above. Given that the maximum SSTs in the warm pool of the CGCM are rather comparable to the observed

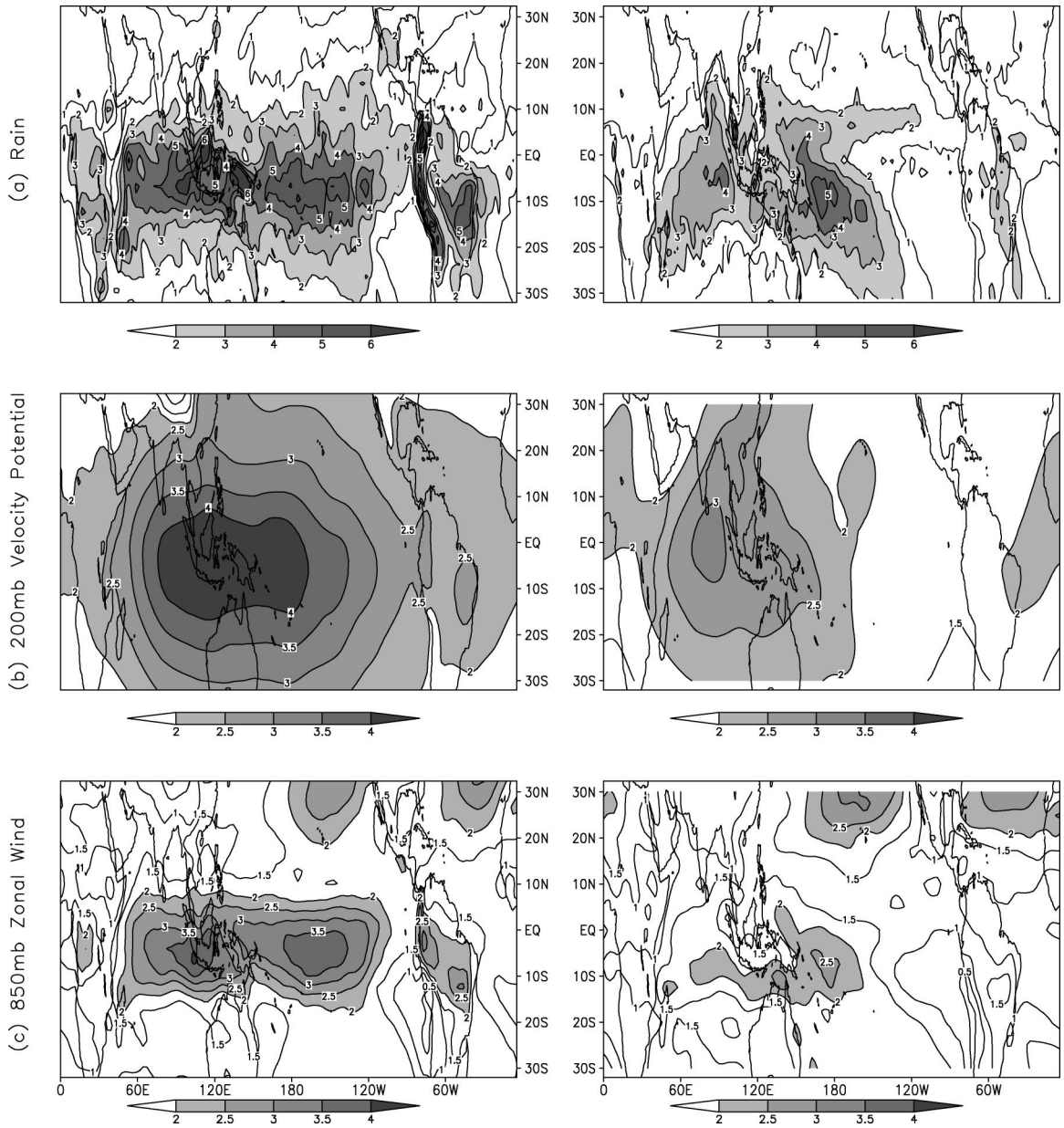

FIG. 4. Std dev of filtered (30–90 days) intraseasonal (a) rain rate, (b) VP200, and (c) U850 from (left) CGCM simulation and from (right) observations for the winter period (Nov–Apr). The model fields are from the years 1979 through 1997 using the simulations starting in Jul (see section 2). The observed precipitation is from the global pentad CMAP from the period Jan 1979 to Dec 1997. The VP200 and U850 fields are from the NCEP–NCAR reanalysis (Kalnay et al. 1996) from the period 1979 to 1997. Units are mm day^{-1} for rain rate, 1×10^6 m^2 s^{-1} for VP, and m s^{-1} for zonal wind.

values, it is not obvious why the intraseasonal variability is larger in the CGCM (and AGCM, see below) than the observations. Such enhanced intraseasonal variability was found in about 3 of the 10 models analyzed by Waliser et al. (2003a), one of which was the GFDL AGCM. Understanding which aspects of GCMs contribute to strong versus weak intraseasonal variability is presently an area of active research, and there is relatively little in the way of uniform answers/mechanisms (Waliser et al. 2003c). In general, the standard deviation of the above three quantities for winter from the AGCM (not shown) are found to be also quite similar to those from CGCM. The differences that do exist will be elaborated on below with more detailed analysis on the main phenomenon of interest, that is, the dominant TISO mode(s).

Figure 5 is the same as Fig. 4 except for the summer. Similar to the winter case, the filtered variability of the rain rate and 200-mb VP as well as the 850-mb zonal winds is considerably larger (~50%) than those of ob-

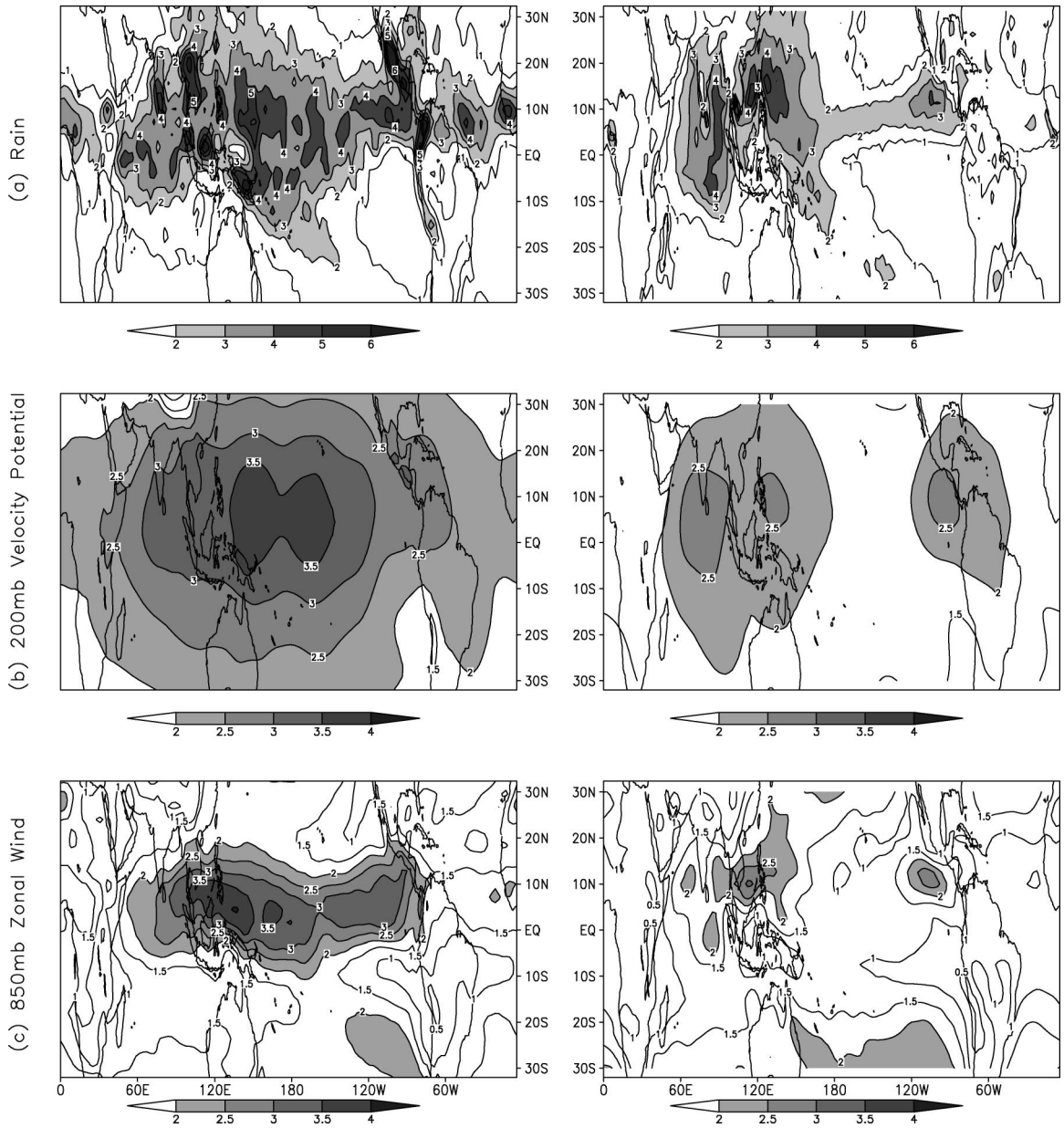

FIG. 5. Same as in Fig. 4, except for the summer (May–Oct) means, for the period 1980 to 1997, and for simulations starting in Jan (see section 2).

servations, especially in the fields of the 200-mb VP and 850-mb zonal winds. From Figs. 4 and 5, it is seen that the model shows some capability at representing the seasonal modulation of the tropical intraseasonal variability, although not all features within a season are well represented. These discrepancies between the models and observations are not unexpected. However, since the major goal of the current study involves investigating how interactive SSTs affect the modeled TISO, the agreement between the modeled results and observations is not of the highest importance. With these considerations in mind, the results shown above indicate that the inclusion of interactive SSTs does not introduce dramatic changes in the spatial structure and magnitude of the model's generalized intraseasonal variability. However, as discussed in section 3d, the spatial structure of the model TISO (i.e., the dominant mode of intraseasonal variability) does undergo some important changes. It is noteworthy that, in each case illustrated above, these filtered standard deviation fields, to a certain extent, resemble their corresponding mean tropical structure indicated in Figs. 1 and 2. Therefore, the variability in these fields within this frequency range tends to be the largest where the mean values are largest and

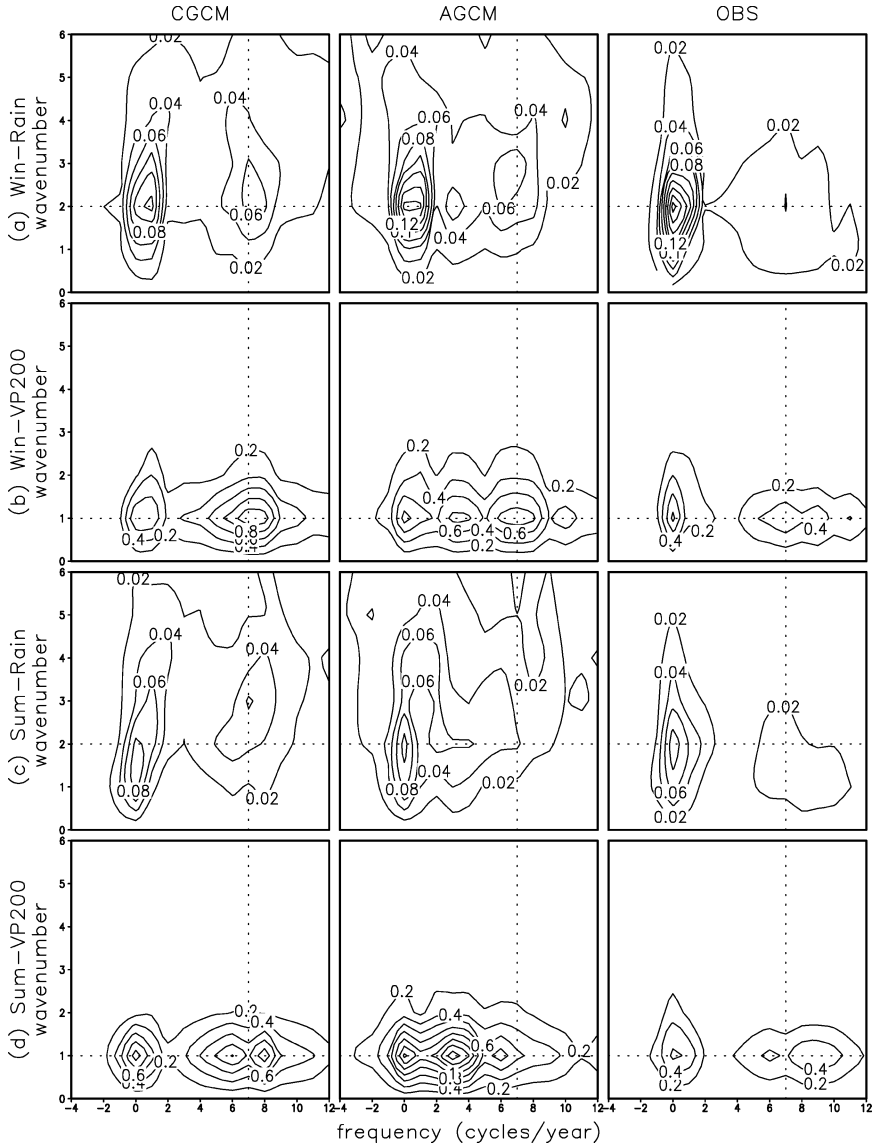

FIG. 6. Wavenumber–frequency power spectra computed from equatorial (10°N–10°S) time–longitude data: (a) rain rate during winter, (b) VP200 during winter, (c) rain rate during summer, and (d) VP200 during summer from (left) the CGCM, (middle) the AGCM, and (right) the observations. Vertical thin dotted lines denote 7 cpy and horizontal thin dotted lines denote wavenumber-2 for rain rate and wavenumber-2 for VP200. Units are $mm^2\ day^{-2}$ for rain-rate variance and $10^{12}\ m^4\ s^{-2}$ for VP variance. See section 3c for details.

vice versa. Compared with the winter case, the filtered variability from the AGCM simulation for summer (not shown) exhibits some modest differences from the CGCM. Again, the similarity between the CGCM and AGCM mean fields indicates that the changes in the features of the modeled TISO to be discussed in the following subsection are probably not the results of changes to the mean climate.

c. Power spectra

Figure 6 shows the mean wavenumber–frequency spectra of anomalous rainfall, the 200-mb VP from the CGCM (first column) and the AGCM (second column), and the corresponding observational results (third column). The data starting from July through the following June each year from 1979 through 1997 were used to compute winter (November–April) power spectra. Similarly, the data starting from January to December each year from 1980 to 1997 were used for the summer (May–October) power spectra. Before computing the spectra for a given year, a trapezoid window was applied in time, with the window equal to one over the season of interest (e.g., summer for the January starts). Thus, the winter (summer) spectra do tend to emphasize the

boreal winter (summer) periods. The above spectra were calculated for each year of the anomaly data (about the annual cycle), averaged between 10°N–10°S, and then the mean of the 19 (18) yr of winter (summer) spectra was computed. The upper (lower) two rows show the winter (summer) data. Positive frequency denotes that the wave propagates eastward while negative frequency denotes that the wave propagates westward.

For rainfall, the CGCM exhibits a broad peak at about 7 cycles per year (cpy) and wavenumbers 2–3. This is the case for both the winter (Fig. 6a) and summer (Fig. 6c). In general, the time and space scales of this TISO-like variability in rainfall agree well with the observations (third column), although the magnitude is slightly larger than for the observations, which is consistent with the comparisons in Figs. 4 and 5. Interestingly, the spectra for AGCM exhibits the same intraseasonal peak in variability as the CGCM, although there is an additional peak at about 3 cpy and wavenumbers 2–3. This additional peak does not appear to have an analog in the observations. The characteristics of the rainfall spectra described above, in regards to the agreement (disagreement) between the CGCM (AGCM) and the observations is even more pronounced in the 200-mb VP spectra (Figs. 5b and 5d), although the variability for the 200-mb VP is almost entirely confined to wavenumber 1.

Figure 7 highlights the above spectral results for wavenumber 1 only to illustrate that these differences between the CGCM and AGCM, at around 3 cpy, are statistically significant at a 95% confidence level for both summer and winter mode in terms of rainfall rate and the 200-mb VP. In summary, the spectral structures of the CGCM appear to be closer to observations than those from the AGCM, indicating that the interactive SSTs might play a role in helping to produce TISO variability with the time scales that are more consistent with those found in the observations (e.g., Waliser et al. 1999b).

d. TISO structure

In order to further examine the space–time structure of the TISO within the CGCM and the AGCM, the data are subject to an extended empirical orthogonal function (EEOF) analysis. The analysis is performed on the filtered pentad data for the tropical domain 32°N–32°S and 30°E–150°W. This region was selected since most of the variability in rainfall data associated with the TISO is found in this region (see Figs. 4 and 5). The EEOF analysis was applied, using temporal lags from -5 to $+5$ pentads, separately in the winter and summer data (see section 3c).

Figure 8 displays the spatial–temporal pattern for the first EEOF mode that depicts the characteristics of the typical cycle of the simulated winter and summer TISO for both the CGCM and the AGCM in terms of precipitation. To compactly illustrate the model–data comparison, lags from -5 and -4 pentads were averaged together (denoted as lag $-5 \sim -4$ pentads in Fig. 8), lags from -3 and -2 pentads were averaged together (denoted as lag $-3 \sim -2$ pentads), and so on. Thus, the maps shown in Fig. 8 are separated by two pentads (i.e., 10 days). The first mode for NH winter CGCM captures a little more variance (5.24%) of the time-lagged sequences of the filtered data than AGCM does (5.13%). The first mode for the NH summer CGCM and AGCM contains 4.0% and 3.24% of the variance, respectively. Shown in the maps in Fig. 8 is the general eastward (northeastward) propagation of the rainfall anomalies in the winter (summer) data, which is consistent with observed MJO (TISO) variability.

In order to better characterize the differences between the CGCM and AGCM simulations and compare them to the observations, composite TISO events are computed for each experiment and for the observations. These composites were constructed by averaging the filtered precipitation for all ''events'' that had an EEOF mode-1 time series amplitude greater than 1.0. Note that if time series had a sequence of values occurring above 1.0, then only the maximum value was used to indicate the event. The composite TISO events have a space–time structure similar to Fig. 8. These composites, and thus a comparison of life cycles of observed and modeled TISOs for the winter in terms of rainfall, are shown in Fig. 9. These winter composites include 38 events for the CGCM, 32 events for the AGCM, and 32 events for the observations. For the composite winter TISO events, the variability is mostly confined to the Eastern Hemisphere. For both models and observations, positive anomalies develop in the Indian Ocean, propagate eastward, and decay in the central and eastern equatorial Pacific. The amplitudes of the variability and phase speed of the propagation within the modeled composites are comparable to those of the observations. One of the most significant shortcomings in the model in regard to the winter TISO, however, is its relatively weak (strong) variability exhibited in the warm pool regions of western Pacific (Maritime Continent). It should be noted that the composite amplitude of the variations in precipitation is smaller than that associated with a typical TISO event, given the averaging process.

Figure 10 is the same as Fig. 9 except for NH summer periods. These summer composites include 45 events for the CGCM, 30 events for the AGCM, and 43 events for the observations. It is interesting to find that there is a 50% increase in the number of events in the simulations with the interactive SSTs for this case. The largest variations in the composites are mostly found over regions in the Northern Hemisphere tropical oceans for both simulations and the observations. One of the more striking features for summer TISO events is that the ''waves'' found in the Eastern Hemisphere have a northwest–southeast tilt. To a great extent, both the CGCM and the AGCM capture this salient property. In this regard, interactive SSTs may make no contribution

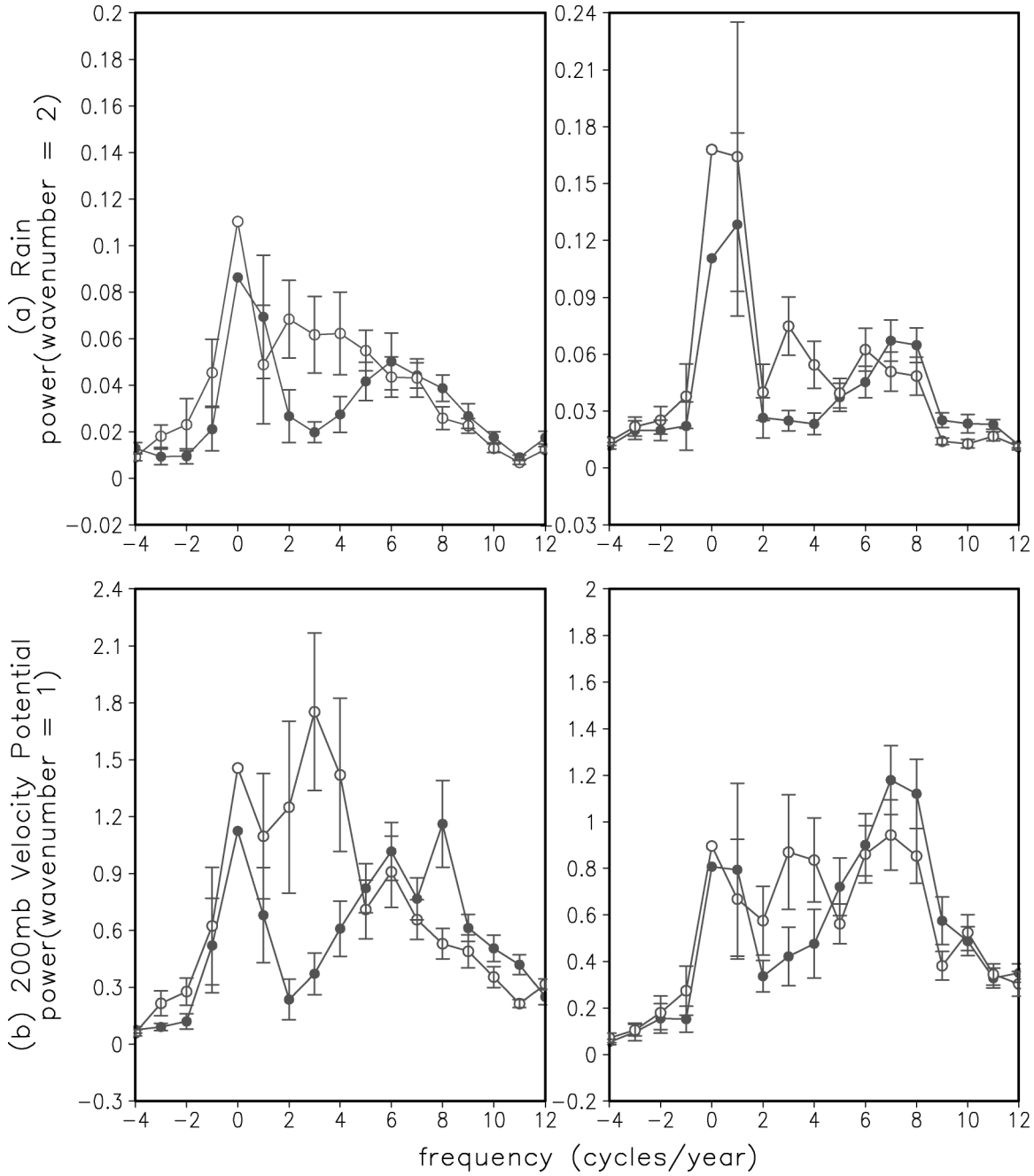

FIG. 7. Power spectra at a given wavenumber taken from data in Fig. 6: (a) wavenumber-2 rain rate, (b) wavenumber-1 VP from the CGCM (solid) and AGCM (open) during the (left) summer and (right) winter. Error bars that do not overlap at a specified frequency denote significant difference in the spectra between the CGCM and AGCM at the 95% confidence level. Units are the same as in Fig. 6.

to this sort of tilt. Similar to the winter composites, the general eastward-propagating speeds in the two simulations are similar to those found in the observations. One of the largest differences between the two simulations is that the CGCM exhibits a larger variability in the eastern Indian Ocean than the AGCM, which agrees better with the observation. On the contrary, for the AGCM, the composite amplitudes over the central Pacific are bigger than those in the CGCM, which is less consistent with the observations. Thus, in regards to each of the above differences, the CGCM appears to exhibit more realistic TISO behavior.

To better highlight the features and differences described above, Fig. 11 shows standard deviation maps associated with the winter composites of the rainfall, 200-mb velocity potential, and 850-mb zonal winds for

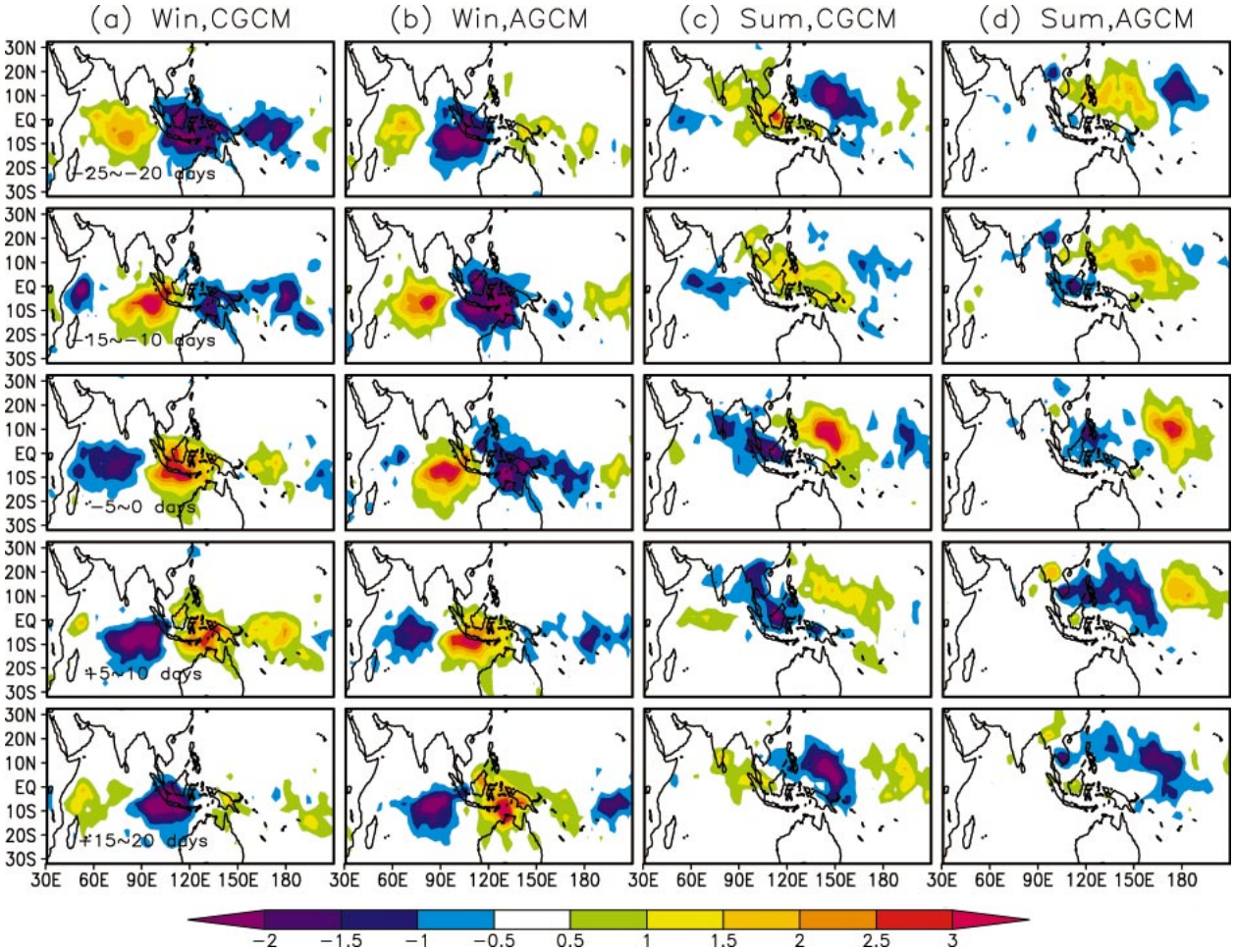

FIG. 8. First mode EEOF of filtered (30–90 days) NH (a) winter (Nov–Apr) rain rate from the CGCM, (b) winter rain rate from the AGCM, (c) summer (May–Oct) rain rate from the CGCM, and (d) summer rain rate from the AGCM for the tropical domain (30°N–30°S, 30°E–150°W). Time lags extend from −25 to −20 days (i.e., −5 and −4 pentads averaged) at the top to +15 to +20 days (i.e., 3 and 4 pentads averaged) at the bottom. Sequential maps are separated by 10 days. Units are mm day^{-1}. See section 3d for details.

the CGCM (left) and the AGCM (right). In order to compare the modeled TISO to the observations, analogous maps for the observations for winter are shown in Fig. 12 (left). Both the CGCM and AGCM have a strong variation in terms of rainfall over the Indian Ocean and southern Maritime Continent regions and a relatively weak variation in the southern subtropical Pacific Ocean, while in the observations (Fig. 12) there is relatively strong variability in this latter region. This large difference is consistent with the results shown in Fig. 9. The strongest variability in the 200-mb VP derived from CGCM and AGCM, which is located over the southern Maritime Continent regions and Indian Ocean, is responsible for the strong variation of rainfall there. This spatial pattern is in excellent agreement with the observations. The spatial patterns of the standard deviation of the 850-mb zonal wind for both models are found to be similar to those found in the 200-mb VP.

Figure 13 is the same as Fig. 11 except for the summer case. The main feature to note here is that the region of strong intraseasonal rainfall variability in the AGCM is almost exclusively limited to the central Pacific Ocean, and there is virtually no intraseasonal variability in the Indian Ocean. This latter feature is a significant shortcoming of the AGCM but one that is rather common (Waliser et al. 2003a). In contrast, the CGCM exhibits considerably more rainfall variability in the Indian Ocean and overall exhibits much better agreement with observations in terms of the spatial extent/pattern of the rainfall variability in this region than is exhibited by the AGCM. The difference in the agreement with observations is even more pronounced for the 200-mb VP field. Both the CGCM and observations exhibit a variability maximum on either side of the Maritime Continent, while the AGCM only exhibits one maximum over the western Pacific. Similarly, the magnitude and pattern of variability in the 850-mb zonal wind in the Indian Ocean is somewhat better represented in the CGCM than in the AGCM, although the region of maximum variability in the CGCM in this region is shifted

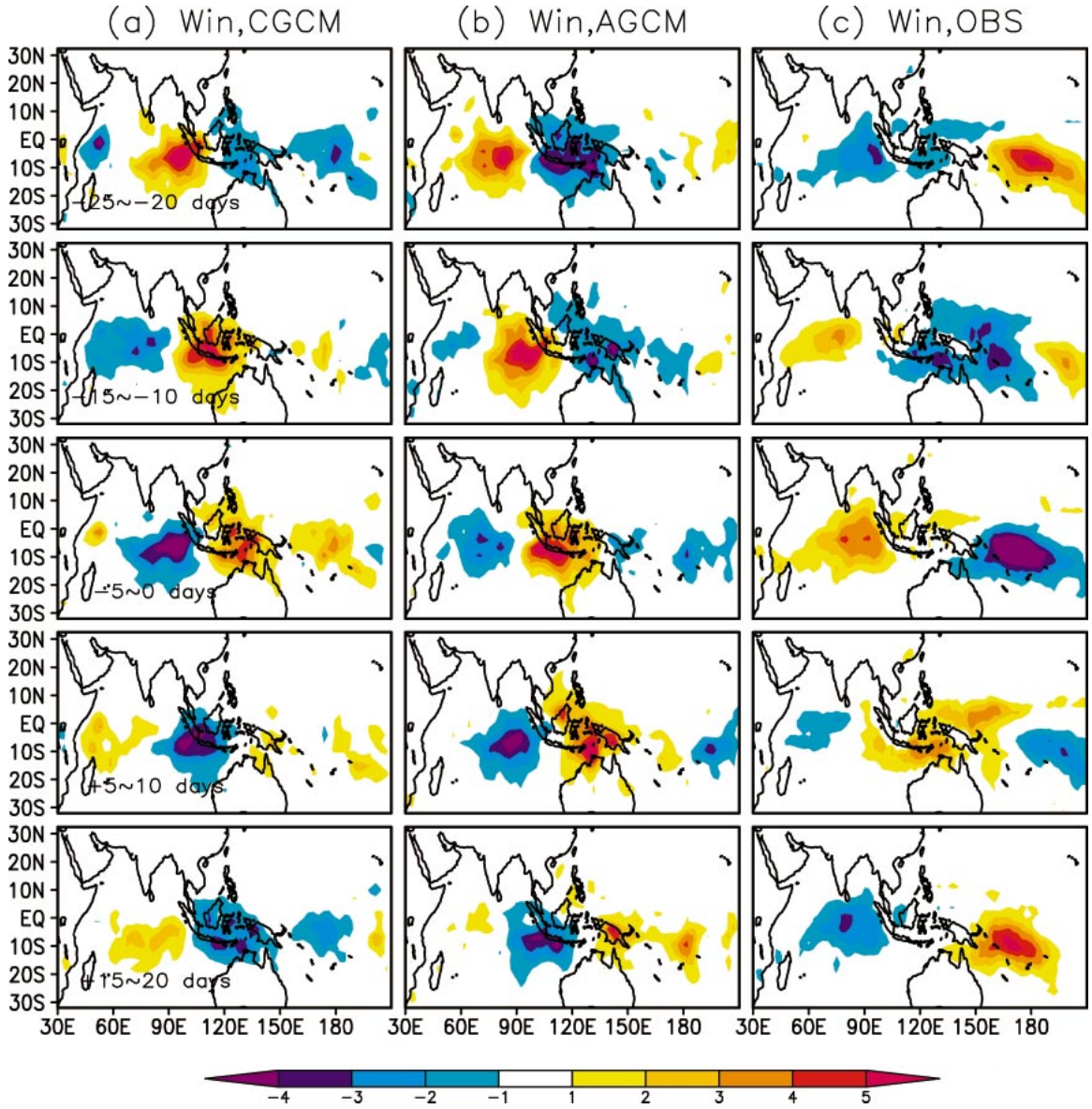

FIG. 9. Composite TISO life cycle in terms of rain rate computed from NH filtered (30–90 days) winter (Nov–Apr) data from (a) CGCM, (b) AGCM, and (c) observations. Lags and units correspond to those used in Fig. 8. See section 3d for details.

southward relative to the observations. Taken together, the analysis above indicates that the CGCM is better at reproducing the summertime rainfall variability in the warm pool regions, particularly the Indian Ocean, than the AGCM.

e. Phase relationships and event locking

To explore the roles of interactive SSTs on the TISO, especially in the regions with a large TISO signal, we investigate the phase relationships between SSTs and TISO in the two model simulations. The regions selected for examination are in the Indian Ocean and western Pacific Ocean where strong TISO variability is prevalent. These regions include the Indian Ocean (0°–15°N, 85°–105°E) and western Pacific Ocean (5°–20°N, 135°–150°E) for the summertime case, and the Indian Ocean (10°S–5°N, 80°–95°E) and western Pacific (10°S–5°N, 130°–145°E) for the wintertime case. For this analysis, the same events identified for inclusion in the 11-pentad TISO composites (Figs. 9 and 10) were used as the basis for calculating the phase relationships. Thus, for the CGCM summer case, there were 30 events identified (the lowest of any of the model/season cases). The spatial average, using the above regions, was computed for the selected events, each of which consists of 11 pentads ($-5, \ldots, +5$ pentad lag). The lagged correlations were then computed from these values, and thus the zero-lag

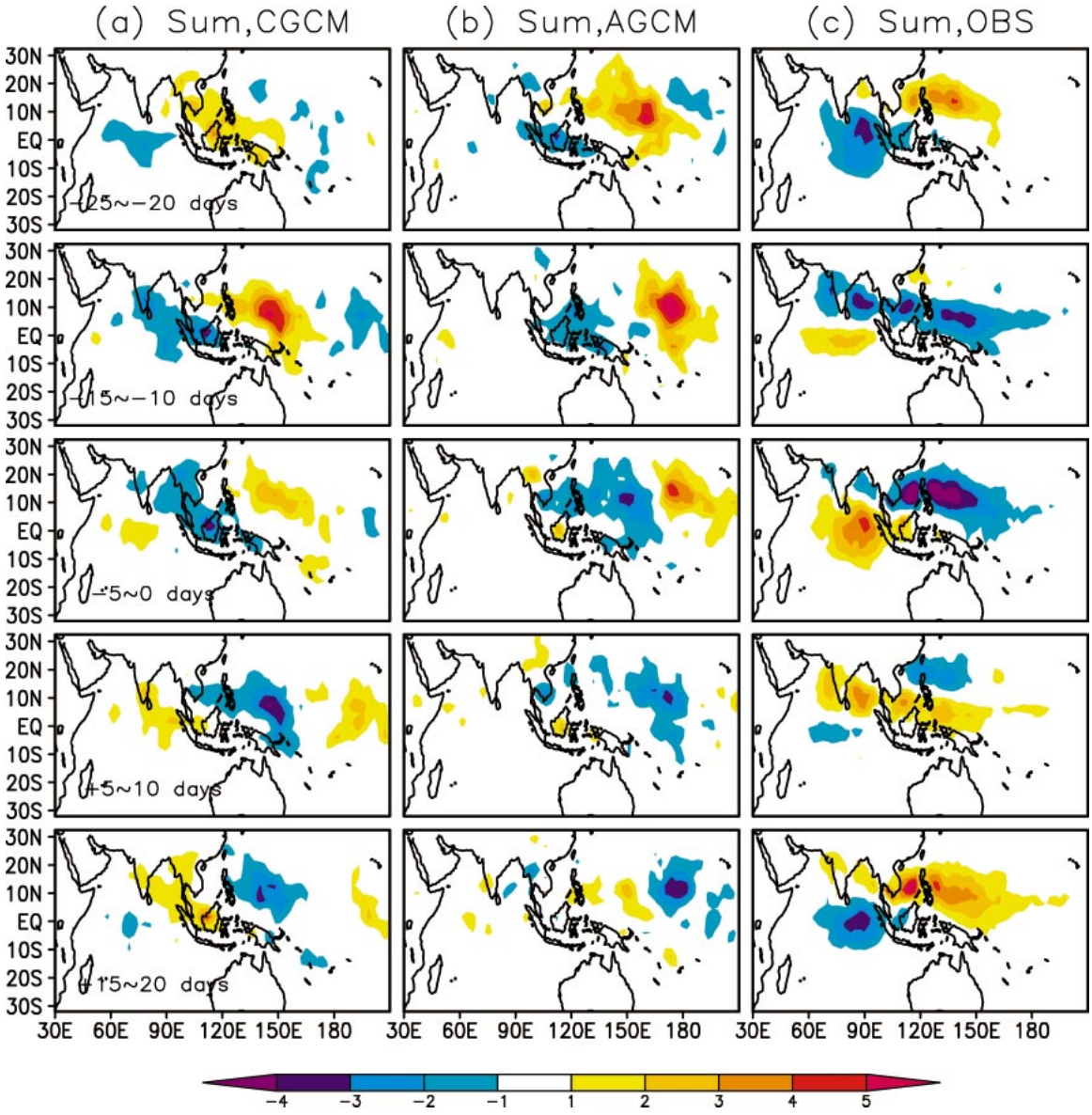

FIG. 10. Same as in Fig. 9, except for NH summer (May–Oct).

calculation includes an N equal to 330. Note that even if one assumes that these samples are not all independent due to the rather fine 5-day resolution and reduces N by a factor of 2 or 3 to account for this, correlations as low as 0.25 are still significant at the 98% level.

Figure 14 shows the results of the lag correlation described above for precipitation and SST, for the selected Indian and western Pacific Ocean regions for both the summer and winter modes. As a general rule, positive SST anomalies lead positive precipitation anomalies in both CGCM and AGCM. In the CGCM, the lag associated with the maximum correlation (~0.7) is about 3 pentads, making the precipitation and SST anomalies in quadrature. This is consistent with observations and is expected because the suppressed (enhanced) convection condition acts to produce warm (cool) SST anomalies (e.g., Vecchi and Harrison 2000; Kemball-Cook and Wang 2001; Sengupta and Ravichandran 2001; Sengupta et al. 2001). It should be mentioned that composites of SST anomalies (not shown), analogous to those of rainfall in Figs. 9 and 10, show that the precipitation and SST anomalies are also in quadrature relative to their spatial orientation, and both propagate northeastward, with the SST leading.

For the AGCM, however, the lag between precipitation and SST anomalies is reduced by about 1–2 pentads (~1 week). This difference can be attributed to the different physical representations in the AGCM and CGCM. In the CGCM, the SST anomalies are produced by the TISO-modulated fluxes, whereby negative (pos-

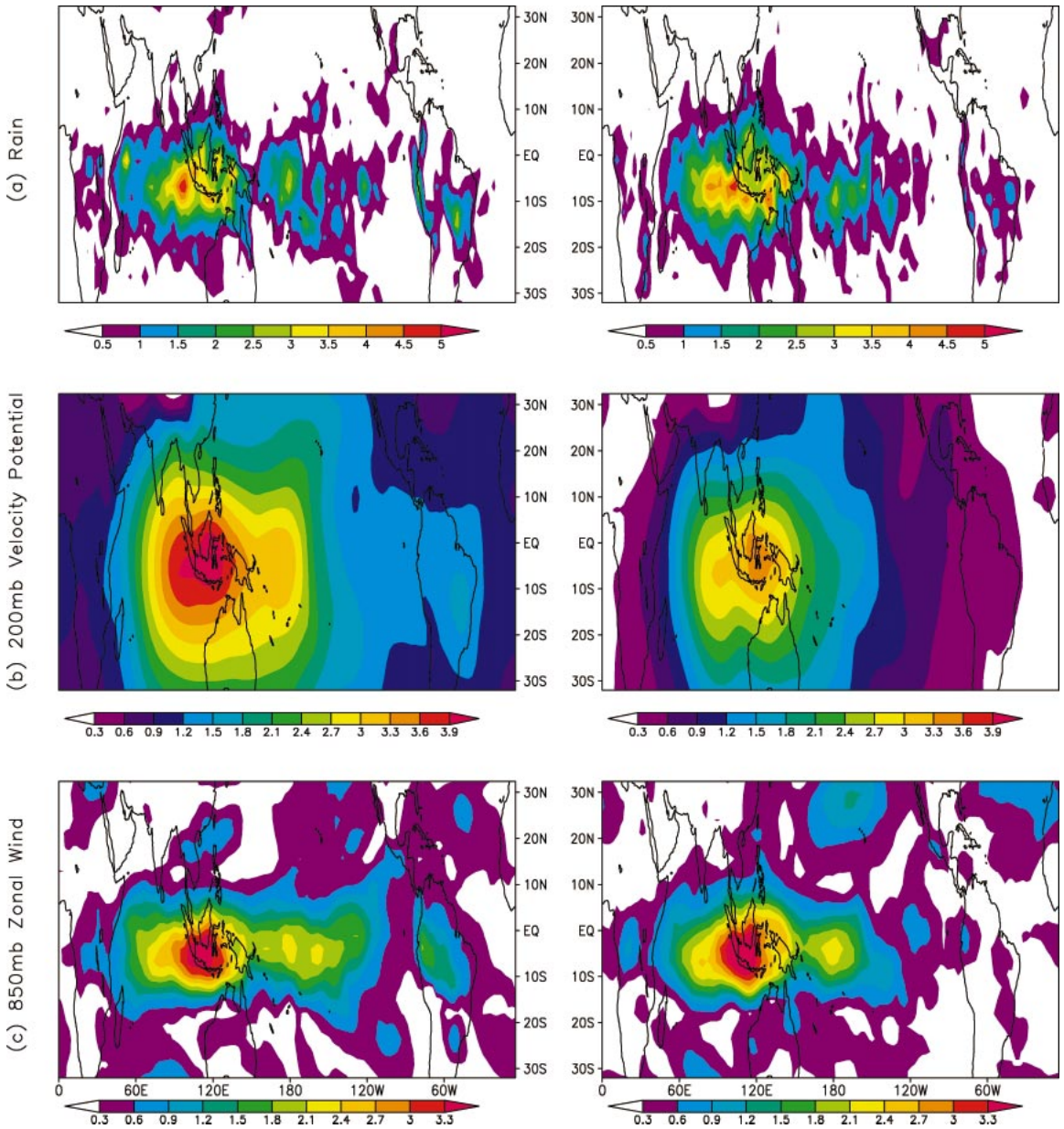

FIG. 11. Std dev of the NH winter (Nov–Apr) composite TISO structure—see Fig. 9 and section 3d—in terms of (a) rain rate, (b) VP200, and (c) U850 from the (left) CGCM and (right) AGCM. The total number of TISO events is 38 for the CGCM and 32 for the AGCM. Units are the same as in Fig. 1.

itive) anomalies in latent heat flux and positive (negative) anomalies of shortwave radiation precede (occur in conjuction and after) the enhanced convection regime and give rise to positive (negative) SST anomalies. The atmospheric component of the system, namely, the convection, continually tries to adjust itself by moving the convection over a warm SST anomaly, the most favorable location, but in so doing causes the SST anomaly itself to propagate, which keeps the convection and SST in quadrature. On the other hand, in the AGCM, the TISO-modulated fluxes have no influence on the SST, although the anomalies are still present. The convection can thus adjust to a location where the SST is more favorable (i.e., nearly in phase) and then the two anomalies can still propagate together. The implications of this difference in phase lag, which amounts to a serious shortcoming in the AGCM, will be discussed in the summary.

To further illustrate the difference in phase relationships between TISO-related precipitation and SST variability illustrated in Fig. 14, as well as to investigate the degree to which the events in the AGCM are forced

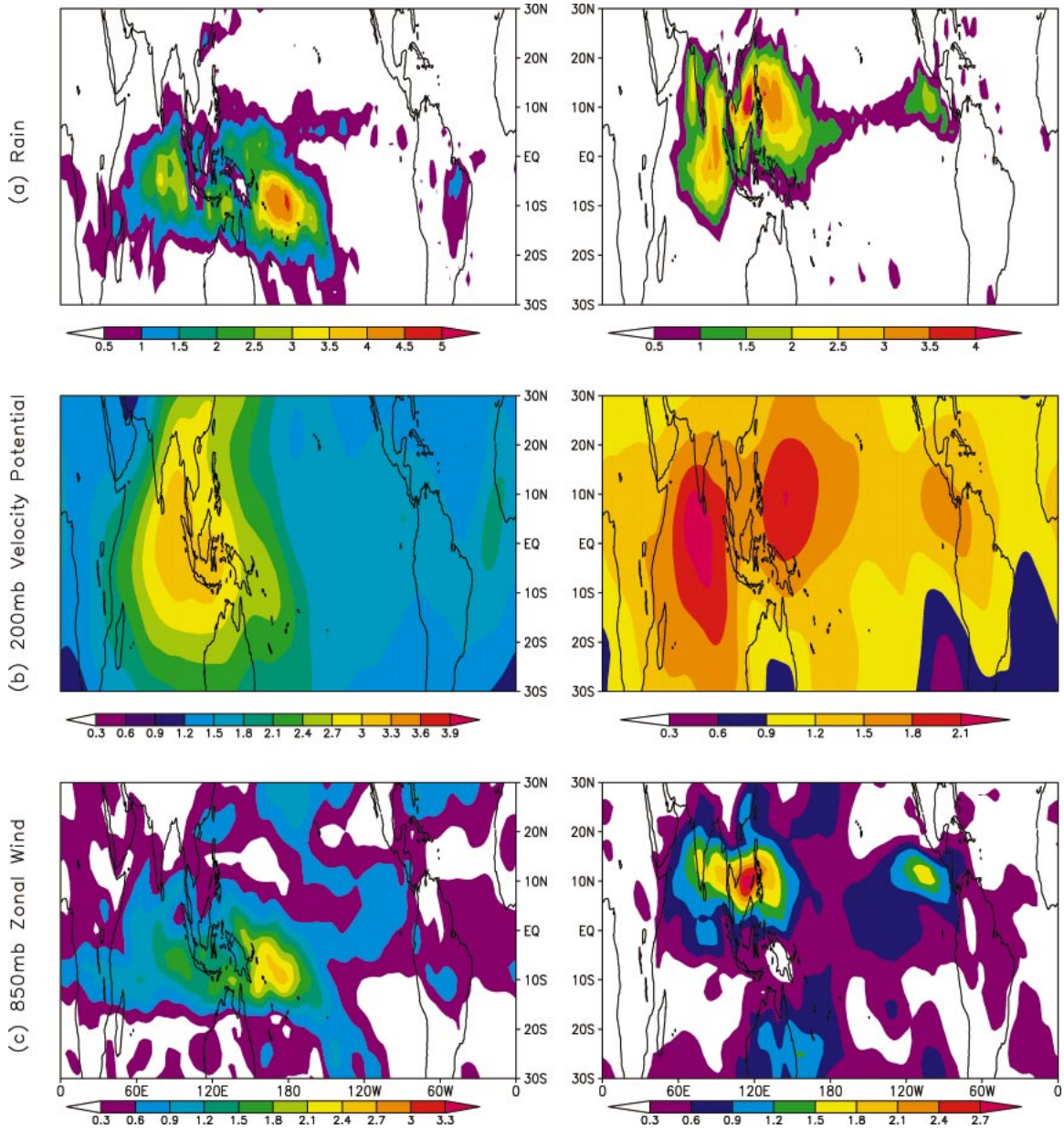

FIG. 12. Std dev of the composite TISO structure—see Fig. 9 and section 3d—for the NH (left) winter (Nov–Apr) and (right) summer (May–Oct) in terms of (a) rain rate, (b) VP200, and (c) U850 from the observations. The total number of TISO events is 32 for winter and 43 for summer. Units are the same as in Fig. 1.

via the imposed intraseasonal SST variations, we examine the extent to which the TISO events from the CGCM and AGCM simulations overlap in time. In order to develop a common reference time series for the identification of events and their relative timing, amplitude time series were constructed for both the AGCM and CGCM simulations and for each season, using the first mode EEOF structure from the AGCM simulations in one case and the EEOF structure from the CGCM in another case. It is necessary to use a common EEOF structure in this analysis since the TISO phasing (e.g., the location of the convection at say lag 0) is, not unexpectedly, represented differently in the CGCM and AGCM EEOF structures (see Fig. 8). The analysis was done with CGCM and AGCM EEOF structures separately just to ensure the results obtained were not dependent on the choice of the EEOF structure used to identify the TISO. As was done in section 3d, the events were identified from the time series maxima that had an amplitude greater than one standard deviation. Table 1 shows the number of events identified from each set of simulations, for each season, and delineated based

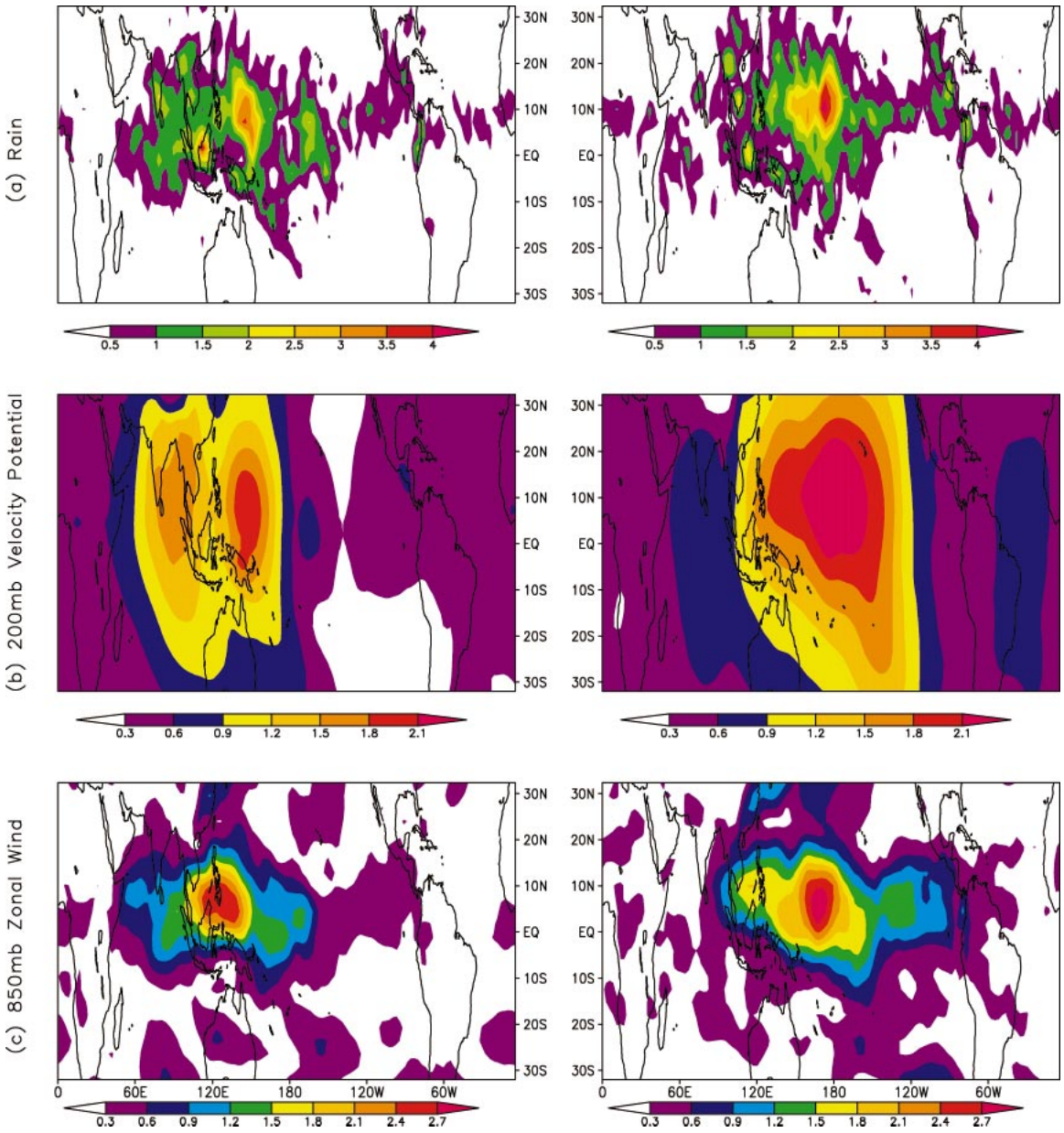

FIG. 13. Same as in Fig. 11, except for the NH summer (May–Oct). The total number of TISO events is 45 for the CGCM and 30 for the AGCM.

on which EEOF (AGCM or CGCM) was used to identify the events. The values denoted with asterisks indicate the same TISO events used to construct the composites in section 3d.

The bar charts in Fig. 15 illustrate the results of the above analysis, with the upper (lower) panel showing the results for the case when the AGCM (CGCM) EEOF was used to identify TISO events. The bars indicate the number of CGCM and AGCM TISO events that appeared to be coincident, or nearly so, in time over the course of the two integrations, with the values on the *x* axis indicating the time lag between the ''common'' events; positive time lags indicate that the event in the AGCM simulation leads the event in the CGCM simulation. Note that only common events that occurred within the time lags shown are indicated on the figure. There are two important aspects to note about the results of this analysis. First, consistent with the lagged-correlation analysis described above, the events in the AGCM simulation that are in common with the CGCM events lead the latter by about 1–2 pentads. Second, of all the events that occurred in the two simulations (i.e., Table 1), a significant fraction of them are nearly coincident in time. For example, examining Fig. 15 (top),

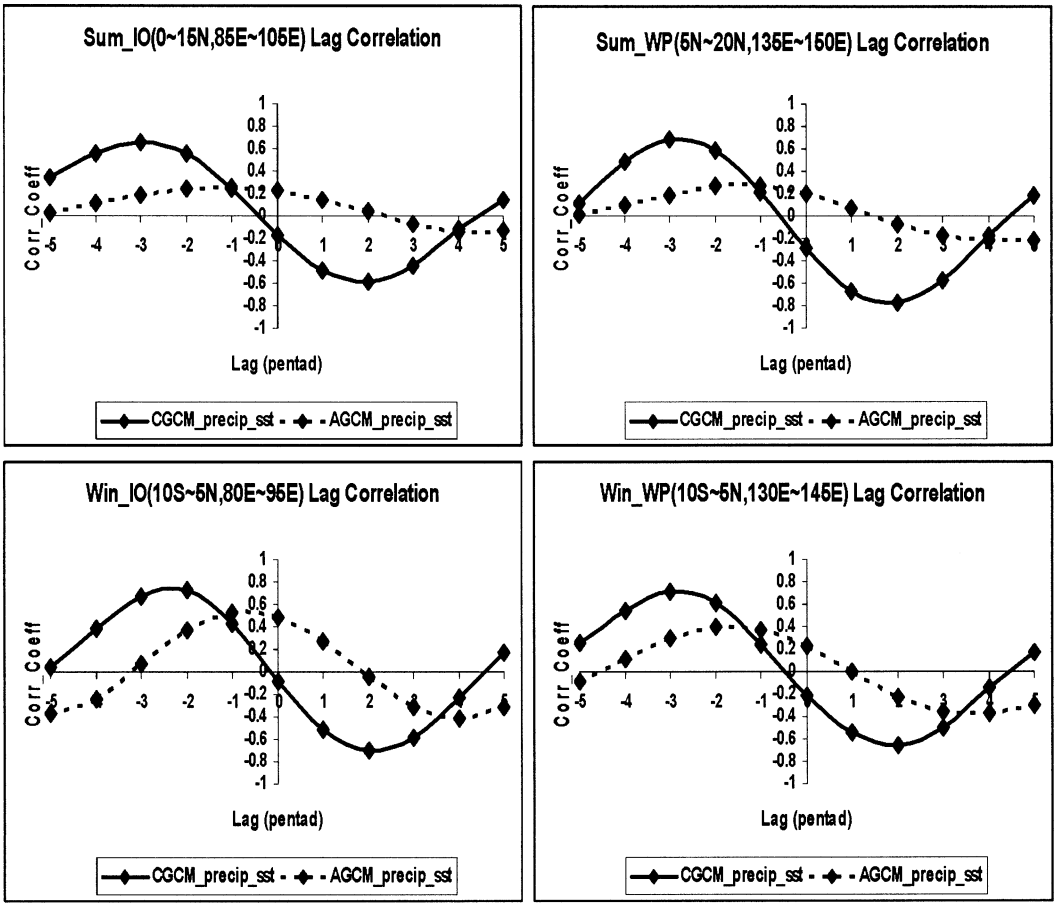

FIG. 14. Lagged correlation diagrams between precipitation and SST averaged over selected regions of the TISO composite—see Fig. 8 and section 3d—from the CGCM (solid) and AGCM (dotted) during the (top) summer and (bottom) winter. Regions selected are denoted in the upper part of each panel. The lagged correlation is made based on the $N \times 11$ points of precipitation and SST averaged over the selected regions, where N is the number of TISO events identified from AGCM and CGCM simulations for both summer and winter. The values of N are 30, 45, 32, and 38 for AGCM summer, CGCM summer, AGCM winter, and CGCM winter, respectively. Also see Table 1.

the case in which the AGCM EEOF was used to identify the TISO events shows that approximately 15–20 events are nearly coincident between the AGCM and CGCM simulations, which from the upper two rows of Table 1 can be seen to represent about 50% of the TISO events of either simulation. A similar examination of Fig. 15 (bottom) and lower two rows of Table 1 shows in that case about 25%–50% of the events in common. Either way, this indicates that there are a considerable number of TISO events that are nearly coincident in time in the CGCM and AGCM simulations.

TABLE 1. Number of TISO events identified from the AGCM and CGCM simulations, for both summer and winter, delineated by the EEOF (AGCM or CGCM) used to identify the events. The values denoted with asterisks indicate the same TISO events used to construct the composites in section 3d.

EEOF from AGCM	CGCM	AGCM
Summer	27	30*
Winter	33	32*
EEOF from CGCM		
Summer	45*	18
Winter	38*	28

It should be stressed that these coincident events do not stem from the CGCM and AGCM having identical initial conditions, given that summer (winter) TISO events are analyzed from integrations starting in January (July), but rather from their *similar* SST boundary conditions (see section 2 and discussion in the following section). This indicates that a large fraction of the TISO events in the AGCM simulation tend to be forced or at least organized by the anomalies in the SST boundary conditions. In addition, the size of the fraction provides some measure of, at least for this model, the sensitivity of TISO initiation and/or evolution to small variations in SST. In and of itself, the notion of having forced TISO events occur in the AGCM simulation is not problematic. In fact, in a forecast setting, it could be desirable. However, since they do not mimic the nature of

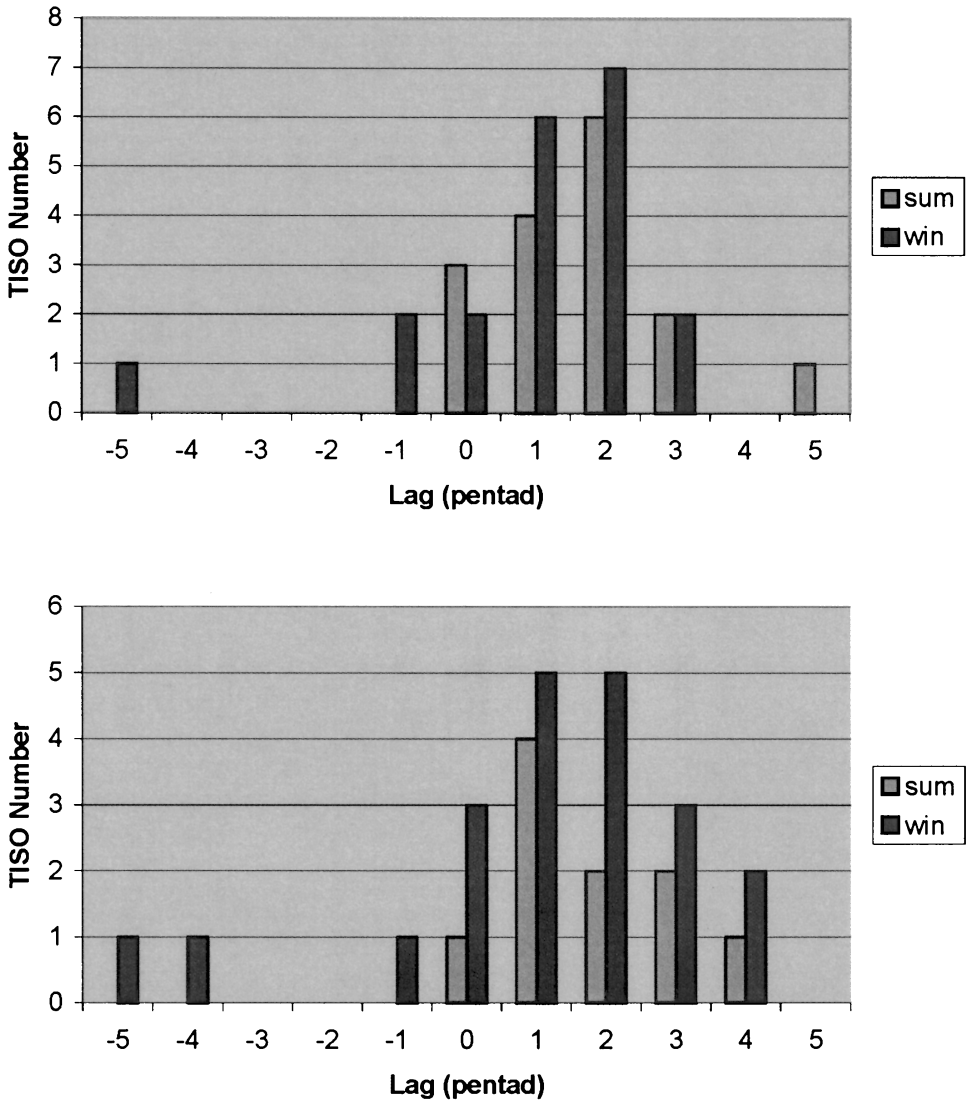

FIG. 15. Number of common TISO events with the given lag based on identification via mode-1 EEOF (see Fig. 8) from the (top) AGCM and (bottom) CGCM for both summer (light) and winter (dark). See section 3e.

the coupled events (e.g., phase lag), their utility in representing the observed TISO or serving as a proxy for the coupled model's TISO is likely to be limited.

4. Summary and conclusions

There has been growing interest in investigating the impacts of SSTs on the atmospheric TISO. Over the last decade, a number of observational studies have indicated that air–sea interaction might play a role in maintaining the MJO (see references in the introduction). More recently, a number of numerical and theoretical modeling studies have explored this issue (see references in the introduction). The outcome of these studies has been highly model dependent, although most of them have supported the idea that the atmospheric TISO can be better simulated/represented when AGCMs include SST coupling. Given the model-dependent nature of the above results, their tendency to focus on either summer or winter seasons but not both, and, for the most part, their reliance on relatively simple ocean-coupling scenarios, this study attempts to extend this line of research by using a different GCM, a framework that includes a fully coupled AGCM and OGCM (i.e., CGCM) and an analysis of both summer and winter seasons. In particular, we use a recent version of the GFDL AGCM that has been shown to exhibit relatively robust intraseasonal variability (Waliser et al. 2003a). The TISO–SST coupling issue is explored by examining the TISO variability in the CGCM and comparing it to the TISO variability in the AGCM when forced with the daily SSTs from the CGCM simulation (see section

2). This experimental design ensures that any differences associated with the TISO between the CGCM and AGCM stemmed only from the coupling and not a change in the background states.

The results show, as intended, that both the CGCM and AGCM produce nearly identical mean climates (Fig. 3). The spatial patterns of the models' climatologies are in rough agreement with observations (Figs. 1 and 2), although there are a number of significant systematic biases associated with the model(s) that warrant caution in extending the results discussed below to the observed system (see section 3a; Figs. 1 and 2). In addition, both models exhibit intraseasonal variability that is about 30% stronger than the observations (Figs. 4 and 5), and while most characteristics of their intraseasonal variability are similar—and also in rough agreement with observations (see section 3b)—there are three noteworthy differences between the AGCM and CGCM simulations. The first of these is the presence of a significant but unrealistic peak in variability in the wavenumber frequency spectra of tropical rainfall, VP200, and U850 in the AGCM that is not evident in either the CGCM or the observations (Figs. 6 and 7). This peak of variability occurs at around wavenumbers 1–3 (depending on the variable) and 3 cpy.

The reason for the presence of this erroneous variability is unclear. Analysis was performed to try and understand the nature of this variability by filtering the individual 2D spectra computed from each year's equatorial time–longitude data to only retain this part of the signal and then inverse transforming. Examination of the results (i.e., filtered equatorial time–longitude diagrams) revealed that there is significant interannual variability regarding this component of low-frequency variability in the AGCM. It is strongest in the region between the Indian Ocean and the eastern Pacific Ocean, with a couple of years having a maximum around the date line. There does not seem to be an obvious correlation to ENSO variability, with relatively high amounts of variability in VP200 in the winters (based on the simulations starting in July) of 1986, 1987, 1994, and 1997; modest amounts in 1984, 1993, and 1995; and nearly absent otherwise. There is a rough correspondence between rainfall and VP200 in this time–space scale, although a few more years seem to be relatively more active in rainfall than VP200. It seems likely that when the model is not run in coupled mode, there are elements of its adjustment process that cannot be accommodated in the same manner as when the system is fully coupled, and that the natural modes of its coupled and uncoupled variability might be different. The above result may not be entirely model dependent as a similar erroneous peak of variability was found in simulations using the NCEP AGCM that was not apparent in the CGCM counterpart (Wang et al. 2004). In that case, however, they are thought to arise from low-frequency variability in the observed specified SSTs, a possibility that is unlikely to account for the difference described here.

The second characteristic involves the spatial pattern of the variability in the principal TISO modes of the CGCM and AGCM—identified via extended empirical orthogonal function (EEOF) analysis. For the austral summer, both the CGCM and AGCM exhibit fairly realistic (too much) TISO variability in the Indian Ocean (Maritime Continent). In regard to the western Pacific, both models tend to underestimate the amount of TISO variability, although the CGCM does exhibit a modest enhancement/improvement over the AGCM (Figs. 11 and 12). For the boreal summer, both the CGCM and AGCM exhibit a fairly realistic amount of TISO variability in the northwestern tropical Pacific (Figs. 12 and 13). However, the AGCM, unlike the observations, exhibits almost no variability in the Indian Ocean. This shortcoming appears to be one of the most ubiquitous features in (fixed SST) AGCM representations of the boreal summer TISO (Waliser et al. 2003a). The CGCM, on the other hand, does show a significant improvement in the amount of variability exhibited in this region, suggesting that SST coupling may be one important process for proper simulation of this feature. Also noteworthy in regard to this portion of the analysis is that the CGCM exhibited 20% (50%) more strong TISO events during the austral (boreal) summer than the AGCM as identified via a threshold value (= one standard deviation) on the time series amplitude of the first EEOF mode. This is an indication that the coupling process may help to produce stronger and more organized events (e.g., Flatau et al. 1997; Waliser et al. 1999b).

The third notable difference between the TISO variability in the CGCM and AGCM simulations is that there is a considerable difference in the phase relationship between TISO anomalies of rainfall and SSTs (Figs. 14 and 15). In the CGCM simulation, there is a near-quadrature relation between TISO-related precipitation and SST anomalies, with the former lagging by about 3 pentads. This quadrature relationship is consistent with that found in observations (see citations in the introduction). In the AGCM, this lag is reduced by about 1.5 pentads, or about a week. This change in the phase relationship between rainfall and SSTs highlights the fundamental nature of the interactive SSTs and their relation to TISO convection anomalies. In the CGCM, and in the observations, the SST anomaly is produced by the TISO-modulated fluxes and continues to remain ahead of the convection in the region where positive ocean heating anomalies have been acting. As the TISO precipitation attempts to adjust to the new anomaly by propagating, the anomaly itself propagates. In contrast, in the AGCM case, the flux anomalies have no impact on the SST and the convection anomalies can move and stay in the SST regime that is more favorable (i.e., closer to the actual positive SST anomaly).

The difference in phase relationship between the

CGCM and AGCM strongly suggests that so-called ''perfect SST'' experiments (whereby observed SST is used in a hindcast setting) or ''two tier'' predictions (whereby a predicted SST from a coupled model is specified as a fixed boundary condition to an AGCM forecast; e.g., Goddard et al. 2001) should not be considered for performing extended-range weather and/or short-term climate hindcasts. In either case, such a framework would embed temporal and spatial phase errors into the large-scale tropical convection field, which, as discussed in the introduction, could impact the extratropics as well. In fact, the results here, as do those of Wu et al. (2002) and Fu and Wang (2004), indicate that there is no SST boundary condition other than a coupled one that will adequately depict the timing/evolution of the TISO relative to the intraseasonal SST anomalies. Moreover, the other two notable shortcomings mentioned above in regard to the AGCM's representation of the TISO further warrant strong consideration for including interactive SSTs in weather/climate forecasts that hope to take full advantage of the slow variation and modulating effects of the MJO/ISO (e.g., Ferranti et al. 1990; Waliser et al. 1999a, 2003b,c,d; Jones et al. 2000; Hendon et al. 2000).

The discussion above has principally stressed three fundamental differences between the AGCM and CGCM TISO representations. For the wave-frequency spectra and phase relationship differences, the enhancements associated with coupling held for both the boreal summer and winter cases. However, for the improvement regarding the spatial variability associated with the TISO, it is not clear why the coupling impact was more evident for the boreal summer case. Or, put another way, why is the AGCM representation of the winter case less problematic in this regard than the summer case? Careful examination of Figs. 11 and 12 does show some enhancements in structure of the variability in upper-level velocity potential and low-level winds, mainly in the western/central Pacific and central/western Indian Ocean. However, the impact is very modest, and combined with the fact that the shortcoming found in the AGCM for boreal summer was identified as such a pervasive problem in a recent AGCM intercomparison study (Waliser et al. 2003a), only the boreal summer case was stressed here. Does this imply that coupling is more important for the boreal summer case? Considering the overall results from this study, and not just this one metric, one would clearly argue that coupling is important for both summer and winter seasons. However, even when considering the improvements associated with coupling highlighted here, and those cited in related studies, it still appears that coupling only leads to improvements in a TISO simulation that is already somewhat realistic. SST coupling will not likely produce a realistic TISO simulation from a nonexistent, very weak, or very poor AGCM simulation of the TISO as 1) the basic instability would still appear to lie within the atmosphere (Waliser et al. 1999b); 2) the magnitude/phasing of the surface flux perturbations associated with the MJO have to be properly represented, of which a large responsibility for this resides in the AGCM (e.g., Maloney and Kiehl 2002); and 3) the model's basic state has been found to play an important role (e.g., Hendon, 2000; Kemball-Cook et al. 2002; Inness et al. 2003; Waliser et al. 2003a).

We would like to stress that the differences found in this study between the CGCM and AGCM are considerable under the condition that the SSTs were the same in the two model simulations. Again, this was done to ensure that any resulting changes in the TISO characteristics between the two models could be readily attributed to the coupling process working within the CGCM, rather than to the background climate of the two simulations or the SST perturbations. However, there is one important caveat that warrants discussion. As indicated in section 2, the SST variations in the CGCM included diurnal variations (2-h steps), while that for the AGCM used daily average SST values. Thus, it is possible that some of the differences in TISO variability noted above could stem from a rectification of the possibly enhanced diurnal variability in the CGCM, which was not present in the AGCM, onto the intraseasonal time scale. This could happen if the manner in which convective instability was acquired and released over the ocean differed in simulations that had modest differences in the amount of diurnal variability.

While diurnally resolving model output was not available for the models used in this study, we did examine the nature and size of the diurnal precipitation and SST variability in the equatorial Indian and western Pacific Oceans from the follow-on version to this model that was constructed to be a relatively close analog. Important to note is that the first few layers of the ocean model have a relatively similar structure, with the first layer having a thickness of about 10 m. For this model and in the warm pool regions, the SST fluctuations include diurnal variations on the order of ± 0.1°C in the midst of intraseasonal fluctuations on the order of ± 0.5°C. However, while the precipitation undergoes intraseasonal fluctuations on the order of ± 20 mm day^{-1}, there are very few systematic diurnal variations associated with these diurnal SST fluctuations. Even during periods of suppressed TISO-related convection, when the SST fluctuations are quire clear and robust, the diurnal fluctuations in precipitation are very weak ($\sim \pm 1$ mm day^{-1}). Thus, while it cannot be ruled out that the difference in diurnal nature of the SSTs in the two experiments could have influenced their differences at the TISO time scale, the possibility seems unlikely.

Finally, it was our hope that a third, intermediary simulation could have been performed whereby the SSTs for the AGCM simulation would have had the intraseasonal variability removed. Such a simulation would have been useful to determine how such SST variability, whether coupled or not, might influence the overall amount of TISO variability and the phase speed

of the TISO propagation (e.g., Flatau et al. 1997; Wang and Xie 1998; Waliser et al. 1999b). Unfortunately, the supercomputer with which this (now obsolete) version of the model was compatible was decommissioned before this simulation could be performed, and while attempts were made to make the source code compatible with the new platform, it was not possible to do within the scope and time frame of this study.

Acknowledgments. Support for this study was provided by the National Science Foundation under Grants ATM-0094416 (DW, YZ) and ATM-0094387 (CJ), by the National Atmospheric and Aeronautics Administration under Grant NAG5-11033 (DW), and, by the National Oceanographic and Atmospheric Administration under Grant NA16GP2021 (DW). The foundation of this study stems from the first author's M.S. thesis at the State University of New York at Stony Brook. This study's analysis and presentation benefited from the use of the GrADS Graphics Package and Seaspace Corporation's TeraScan software system.

REFERENCES

Annamalai, H., and J. M. Slingo, 2001: Active/break cycles: Diagnosis of the intraseasonal variability of the Asian Summer Monsoon. *Climate Dyn.,* **18,** 85–102.

Chang, C. P., and H. Lim, 1988: Kelvin wave-CISK: A possible mechanism for the 30–50 day oscillations. *J. Atmos. Sci.,* **45,** 1709–1720.

Chou, S.-H., C.-L. Shie, R. M. Atlas, and J. Ardizzone, 1995: The December 1992 westerly wind burst and its impact on evaporation determined from SSMI data. *Proc. Int. Scientific Conf. on the Tropical Ocean Global Atmosphere Program,* Melbourne, Australia, World Meteorological Organization, 489–493.

Duchon, C. E., 1979: Lanczos filter in one and two dimensions. *J. Appl. Meteor.,* **18,** 1016–1022.

Emanuel, K. A., 1987: An air–sea interaction model of intraseasonal oscillations in the Tropics. *J. Atmos. Sci.,* **44,** 2324–2340.

Fasullo, J., and P. Webster, 1995: Aspects of ocean/atmosphere interaction during westerly wind bursts. *Proc. Int. Scientific Conf. on the Tropical Ocean Global Atmosphere Program,* Melbourne, Australia, World Meteorological Organization, 39–43.

Ferranti, L., T. N. Palmer, F. Molteni, and K. Klinker, 1990: Tropical–extratropical interaction associated with the 30–60-day oscillation and its impact on medium and extended range prediction. *J. Atmos. Sci.,* **47,** 2177–2199.

Flatau, M., P. J. Flatau, P. Phoebus, and P. P. Niiler, 1997: The feedback between equatorial convection and local radiative and evaporative processes: The implications for intraseasonal oscillations. *J. Atmos. Sci.,* **54,** 2373–2386.

Fu, X., and B. Wang, 2004: Differences of boreal summer intraseasonal oscillations simulated in an atmosphere–ocean coupled model and an atmosphere-only model. *J. Climate,* **17,** 1263–1271.

——, ——, T. Li, and J. McCreary, 2003: Coupling between northward-propagating, intraseasonal oscillations and sea surface temperature in the Indian Ocean. *J. Atmos. Sci.,* **60,** 1733–1753.

Goddard, L., S. J. Mason, S. E. Zebiak, C. F. Ropelewski, R. Basher, and M. A. Cane, 2001: Current approaches to seasonal-to-interannual climate predictions. *Int. J. Climatol.,* **21,** 1111–1152.

Hendon, H. H., 1988: A simple model of the 40–50 day oscillation. *J. Atmos. Sci.,* **45,** 569–584.

——, 2000: Impact of air–sea coupling on the Madden–Julian oscillation in a general circulation model. *J. Atmos. Sci.,* **57,** 3939–3952.

——, and B. Liebmann, 1990a: A composite study of onset of the Australian summer monsoon. *J. Atmos. Sci.,* **47,** 2227–2240.

——, and ——, 1990b: The intraseasonal (30–50 day) oscillation of the Australian summer monsoon. *J. Atmos. Sci.,* **47,** 2909–2923.

——, and M. L. Salby, 1994: The life cycle of the Madden–Julian oscillation. *J. Atmos. Sci.,* **51,** 2225–2237.

——, and J. Glick, 1997: Intraseasonal air–sea interaction in the tropical Indian and Pacific Oceans. *J. Climate,* **10,** 647–661.

——, B. Liebmann, and J. D. Glick, 1998: Oceanic Kelvin waves and the Madden–Julian oscillation. *J. Atmos. Sci.,* **55,** 88–101.

——, ——, M. Newman, J. D. Glick, and J. E. Schemm, 2000: Medium-range forecast errors associated with active episodes of the Madden–Julian oscillation. *Mon. Wea. Rev.,* **128,** 69–86.

Higgins, R. W., and S. D. Schubert, 1996: Simulations of persistent North Pacific circulation anomalies and interhemispheric teleconnections. *J. Atmos. Sci.,* **53,** 188–207.

——, and K. C. Mo, 1997: Persistent North Pacific circulation anomalies and the tropical intraseasonal oscillation. *J. Climate,* **10,** 223–244.

——, and W. Shi, 2001: Intercomparison of the principal modes of interannual and intraseasonal variability of the North American monsoon system. *J. Climate,* **14,** 403–417.

——, J. K. E. Schemm, W. Shi, and A. Leetmaa, 2000: Extreme precipitation events in the western United States related to tropical forcing. *J. Climate,* **13,** 793–820.

Inness, P. M., and J. M. Slingo, 2003: Simulation of the Madden–Julian oscillation in a coupled general circulation model. Part I: Comparison with observations and an atmosphere-only GCM. *J. Climate,* **16,** 345–364.

——, ——, E. Guilyardi, and J. Cole, 2003: Simulation of the Madden–Julian oscillation in a coupled general circulation model. Part II: The role of the basic state. *J. Climate,* **16,** 365–382.

Johnson, R. H., 1995: Variability of clouds and precipitation during TOGA COARE. *Proc. Int. Scientific Conf. on the Tropical Ocean Global Atmosphere Program,* Melbourne, Australia, World Meteorological Organization, 552–556.

Jones, C., 2000: Occurrence of extreme precipitation events in California and relationships with the Madden–Julian oscillation. *J. Climate,* **13,** 3576–3587.

——, and B. C. Weare, 1996: The role of low-level moisture convergence and ocean latent heat fluxes in the Madden and Julian oscillation: An observational analysis using ISCCP data and ECMWF analyses. *J. Climate,* **9,** 3086–3104.

——, and J. K. E. Schemm, 2000: The influence of intraseasonal variations on medium- to extended-range weather forecasts over South America. *Mon. Wea. Rev.,* **128,** 486–494.

——, D. E. Waliser, and C. Gautier, 1998: The influence of the Madden–Julian oscillation on ocean surface heat fluxes and sea surface temperatures. *J. Climate,* **11,** 1057–1072.

——, ——, J. K. E. Schemm, and W. K. M. Lau, 2000: Prediction skill of the Madden and Julian Oscillation in dynamical extended range forecasts. *Climate Dyn.,* **16,** 273–289.

——, L. M. V. Carvalho, W. Higgins, D. Waliser, and J.-K. Schemm, 2004: Climatology of tropical intraseasonal convective anomalies: 1979–2002. *J. Climate,* **17,** 523–539.

Kalnay, E., and Coauthors, 1996: The NCEP/NCAR 40-Year Reanalysis Project. *Bull. Amer. Meteor. Soc.,* **77,** 437–471.

Kang, I.-S., and Coauthors, 2002: Intercomparison of the climatological variations of Asian summer monsoon precipitation simulated by 10 GCMs. *Climate Dyn.,* **19,** 383–395.

Kawamura, R., 1988: Intraseasonal variability of sea surface temperatures over the tropical western Pacific. *J. Meteor. Soc. Japan,* **66,** 1007–1012.

——, 1991: Air–sea coupled modes on intraseasonal and interannual time scales over the tropical western Pacific. *J. Geophys. Res.,* **96,** 3165–3172.

Kemball-Cook, S., and B. Wang, 2001: Equatorial waves and air–sea

interaction in the boreal summer intraseasonal oscillations. *J. Climate,* **14,** 2923–2942.
——, ——, and X. Fu, 2002: Simulation of the ISO in the ECHAM-4 model: The impact of coupling with an ocean model. *J. Atmos. Sci.,* **59,** 1433–1453.
Kessler, W. S., and R. Kleeman, 2000: Rectification of the Madden–Julian oscillation into the ENSO cycle. *J. Climate,* **13,** 3560–3575.
——, M. J. McPhaden, and K. M. Weickmann, 1995: Forcing of intraseasonal Kelvin waves in the equatorial Pacific. *J. Geophys. Res.,* **100** (C3), 4893–4920.
Krishnamurti, T. N., and P. Ardunay, 1980: The 10 to 20 day westward propagating mode and ''breaks in the monsoons.'' *Tellus,* **32,** 15–26.
——, D. K. Oosterhof, and A. V. Metha, 1988: Air–sea interaction on the timescale of 30 to 50 days. *J. Atmos. Sci.,* **45,** 1304–1322.
Lau, K.-M., and P. H. Chan, 1986a: The 40–50 day oscillation and the El Niño/Southern Oscillation—A new perspective. *Bull. Amer. Meteor. Soc.,* **67,** 533–534.
——, and ——, 1986b: Aspects of the 40–50 day oscillation during the northern summer as inferred from outgoing longwave radiation. *Mon. Wea. Rev.,* **114,** 1354–1367.
——, and T. J. Phillips, 1986: Coherent fluctuations of extratropical geopotential height and tropical convection in intraseasonal timescales. *J. Atmos. Sci.,* **43,** 1164–1181.
——, and L. Peng, 1987: Origin of low-frequency (intraseasonal) oscillations in the tropical atmosphere. Part I: Basic theory. *J. Atmos. Sci.,* **44,** 950–972.
——, and C. H. Sui, 1997: Mechanisms of short-term sea surface temperature regulation: Observations during TOGA COARE. *J. Climate,* **10,** 465–472.
Li, T. M., and B. Wang, 1994: The influence of sea surface temperature on the tropical intraseasonal oscillation: A numerical study. *Mon. Wea. Rev.,* **122,** 2349–2362.
Liebmann, B., and D. L. Hartmann, 1984: An observational study of tropical–midlatitude interaction on intraseasonal timescales during winter. *J. Atmos. Sci.,* **41,** 3333–3350.
Madden, R. A., and P. R. Julian, 1971: Detection of a 40–50 day oscillation in the zonal wind in the tropical Pacific. *J. Atmos. Sci.,* **28,** 702–708.
——, and ——, 1994: Observations of the 40–50-day tropical oscillation—A review. *Mon. Wea. Rev.,* **122,** 814–837.
Maloney, E. D., and D. L. Hartmann, 2000a: Modulation of eastern North Pacific hurricanes by the Madden–Julian oscillation. *J. Climate,* **13,** 1451–1460.
——, and ——, 2000b: Modulation of hurricane activity in the Gulf of Mexico by the Madden–Julian oscillation. *Science,* **287,** 2002–2004.
——, and J. T. Kiehl, 2002: Intraseasonal eastern Pacific precipitation and SST variations in a GCM coupled to a slab ocean model. *J. Climate,* **15,** 2989–3007.
McPhaden, M. J., 1999: El Niño—The child prodigy of 1997–98. *Nature,* **398,** 559–562.
——, and B. A. Taft, 1988: Dynamics of seasonal and intraseasonal variability in the eastern equatorial Pacific. *J. Phys. Oceanogr.,* **18,** 1713–1732.
——, H. P. Freitag, S. P. Hayes, B. A. Taft, Z. Chien, and K. Wyrtki, 1988: The response of the equatorial Pacific Ocean to a westerly wind burst in May 1986. *J. Geophys. Res.,* **93** (C9), 10 589–10 603.
Mo, K. C., 2000: Intraseasonal modulation of summer precipitation over North America. *Mon. Wea. Rev.,* **128,** 1490–1505.
——, and R. W. Higgins, 1998a: The Pacific–South American modes and tropical convection during the Southern Hemisphere winter. *Mon. Wea. Rev.,* **126,** 1581–1596.
——, and ——, 1998b: Tropical convection and precipitation regimes in the western United States. *J. Climate,* **11,** 2404–2423.
——, and ——, 1998c: Tropical influences on California precipitation. *J. Climate,* **11,** 412–430.
Nakazawa, T., 1995: Intraseasonal oscillations during the TOGA COARE IOP. *J. Meteor. Soc. Japan,* **73,** 305–319.
Neelin, J. D., I. M. Held, and K. H. Cook, 1987: Evaporation–wind feedback and low-frequency variability in the tropical atmosphere. *J. Atmos. Sci.,* **44,** 2341–2348.
Nogués-Paegle, J., and K. C. Mo, 1997: Alternating wet and dry conditions over South America during summer. *Mon. Wea. Rev.,* **125,** 279–291.
Pacanowski, R. C., 1995: MOM 2 documentation, user's guide and reference manual. GFDL Ocean Group Tech. Rep. 3, 232 pp.
Paegle, J. N., L. A. Byerle, and K. C. Mo, 2000: Intraseasonal modulation of South America summer precipitation. *Mon. Wea. Rev.,* **128,** 837–850.
Sengupta, D., and M. Ravichandran, 2001: Oscillations of Bay of Bengal sea surface temperature during the 1998 summer monsoon. *Geophys. Res. Lett.,* **28,** 2033–2036.
——, B. N. Goswami, and R. Senan, 2001: Coherent intraseasonal oscillations of ocean and atmosphere during the Asian summer monsoon. *Geophys. Res. Lett.,* **28,** 4127–4130.
Shinoda, T., and H. H. Hendon, 1998: Mixed layer modeling of intraseasonal variability in the tropical western Pacific and Indian Oceans. *J. Climate,* **11,** 2668–2685.
——, ——, and J. Glick, 1998: Intraseasonal variability of surface fluxes and sea surface temperature in the tropical western Pacific and Indian Oceans. *J. Climate,* **11,** 1685–1702.
Sikka, D. R., and S. Gadgil, 1980: On the maximum cloud zone and the ITCZ over Indian longitudes during the southwest monsoon. *Mon. Wea. Rev.,* **108,** 1840–1853.
Slingo, J. M., and Coauthors, 1996: Intraseasonal oscillations in 15 atmospheric general circulation models: Results from an AMIP diagnostic subproject. *Climate Dyn.,* **12,** 325–357.
Sobel, A. H., and H. Gildor, 2003: A simple time-dependent model of SST hot spots. *J. Climate,* **16,** 3978–3992.
Sperber, K. R., J. M. Slingo, P. M. Inness, and K. M. Lau, 1997: On the maintenance and initiation of the intraseasonal oscillation in the NCEP/NCAR reanalysis and the GLA and UKMO AMIP simulations. *Climate Dyn.,* **13,** 769–795.
Stern, W., and K. Miyakoda, 1995: Feasibility of seasonal forecasts inferred from multiple GCM simulations. *J. Climate,* **8,** 1071–1085.
Vecchi, G. A., and D. E. Harrison, 2000: Tropical Pacific sea surface temperature anomalies, El Niño, and equatorial westerly wind events. *J. Climate,* **13,** 1814–1830.
Waliser, D. E., 1996: Formation and limiting mechanism for very high sea surface temperature: Linking the dynamics and thermodynamics. *J. Climate,* **9,** 161–188.
——, C. Jones, J. K. E. Schemm, and N. E. Graham, 1999a: A statistical extended-range tropical forecast model based on the slow evolution of the Madden–Julian oscillation. *J. Climate,* **12,** 1918–1939.
——, K.-M. Lau, and J.-H. Kim, 1999b: The influence of coupled sea surface temperatures on the Madden–Julian oscillation: A model perturbation experiment. *J. Atmos. Sci.,* **56,** 333–358.
——, and Coauthors, 2003a: AGCM simulations of intraseasonal variability associated with the Asian summer monsoon. *Climate Dyn.,* **21,** 423–446.
——, K. M. Lau, W. Stern, and C. Jones, 2003b: Potential predictability of the Madden–Julian oscillation. *Bull. Amer. Meteor. Soc.,* **84,** 33–50.
——, S. Schubert, A. Kumar, K. Weickmann, and R. Dole, 2003c: *Proc. Workshop on Modeling, Simulation and Forecasting of Subseasonal Variability,* College Park, MD, NASA, NASA/TM 2003-104606, Vol. 25, 67 pp.
——, W. Stern, S. Schubert, and K. M. Lau, 2003d: Dynamic predictability of intraseasonal variability associated with the Asian summer monsoon. *Quart. J. Roy. Meteor. Soc.,* **129,** 2897–2925.
Wang, B., and H. Rui, 1990: Synoptic climatology and transient tropical intraseasonal convection anomalies—1978–1985. *Meteor. Atmos. Phys.,* **44,** 43–61.
——, and X. Xie, 1998: Coupled modes of the warm pool climate

system. Part I: The role of air–sea interaction in maintaining Madden–Julian oscillation. *J. Climate*, **11,** 2116–2135.

Wang, W., S. Saha, and H.-L. Pan, 2004: Simulation and prediction of the MJO with the NCEP models. *Proc. ECMWF/CLIVAR Workshop on Simulation and Prediction of Intra-Seasonal Variability with Emphasis on the MJO*, Reading, United Kingdom, ECMWF, 14.

Watterson, I. G., 2002: The sensitivity of subannual and intraseasonal tropical variability to model ocean mixed layer depth. *J. Geophys. Res.*, **107A,** 4020, doi:10.1029/2001JD000671.

Webster, P. J., and R. Lukas, 1992: TOGA COARE: The Coupled Ocean–Atmosphere Response Experiment. *Bull. Amer. Meteor. Soc.*, **73,** 1377–1416.

Weickmann, K. M., 1983: Intraseasonal circulation and outgoing longwave radiation modes during Northern Hemisphere winter. *Mon. Wea. Rev.*, **111,** 1838–1858.

——, 1991: El Niño/Southern Oscillation and Madden–Julian (30–60 day) oscillations during 1981–1982. *J. Geophys. Res.*, **96C,** 3187–3195.

——, G. R. Lussky, and J. E. Kutzbach, 1985: Intraseasonal (30–60 day) fluctuations of outgoing longwave radiation and 250 mb streamfunction during northern winter. *Mon. Wea. Rev.*, **113,** 941–961.

Woolnough, S. J., J. M. Slingo, and B. J. Hoskins, 2000: The relationship between convection and sea surface temperature on intraseasonal timescales. *J. Climate*, **13,** 2086–2104.

Wu, M. L. C., S. Schubert, I. S. Kang, and D. E. Waliser, 2002: Forced and free intraseasonal variability over the South Asian monsoon region simulated by 10 AGCMs. *J. Climate*, **15,** 2862–2880.

Xie, P., and P. A. Arkin, 1997: Global precipitation: A 17-year monthly analysis based on gauge observations, satellite estimates, and numerical model outputs. *Bull. Amer. Meteor. Soc.*, **78,** 2539–2558.

Yasunari, T., 1980: A quasi-stationary appearance of the 30–40 day period in the cloudiness fluctuations during the summer monsoon over India. *J. Meteor. Soc. Japan*, **58,** 336–354.

Zhang, C., 1996: Atmospheric intraseasonal variability at the surface in the tropical western Pacific Ocean. *J. Atmos. Sci.*, **53,** 739–758.